PLANT SCIENCES

The epigenetic factor FVE orchestrates cytoplasmic SGS3-DRB4-DCL4 activities to promote transgene silencing in *Arabidopsis*

Di Sun[1†], Yanjun Li[1†], Zeyang Ma[1], Xingxing Yan[1], Niankui Li[1], Baoshuan Shang[1], Xiaomei Hu[1], Kai Cui[1,2], Hisashi Koiwa[3], Xiuren Zhang[1]*

Posttranscriptional gene silencing (PTGS) is a regulatory mechanism to suppress undesired transcripts. Here, we identified *Flowering locus VE* (*FVE*), a well-known epigenetic component, as a new player in cytoplasmic PTGS. Loss-of-function *fve* mutations substantially reduced the accumulation of transgene-derived small interfering RNAs (siRNAs). FVE interacts with suppressor of gene silencing 3 (SGS3), a master component in PTGS. FVE promotes SGS3 homodimerization that is essential for its function. FVE can bind to single-stranded RNA and double-stranded RNA (dsRNA) with moderate affinities, while its truncated form FVE-8 has a significantly increased binding affinity to dsRNA. These affinities affect the association and channeling of SGS3-RNA to downstream dsRNA binding protein 4 (DRB4)/Dicer-like protein 2/4 (DCL2/4) complexes. Hence, FVE, but not FVE-8, biochemically enhances the DRB4/DCL2/4 activity in vitro. We surmise that FVE promotes production of transgene-derived siRNAs through concertedly tuning SGS3-DRB4/DCL2/4 functions. Thus, this study revealed a noncanonical role of FVE in PTGS.

INTRODUCTION

Posttranscriptional gene silencing (PTGS) is a regulatory mechanism that suppresses the expression of endogenous genes while also degrading invasive RNAs such as transgene-derived and viral transcripts. PTGS is guided through microRNAs (miRNAs) and small interfering RNAs (siRNAs) (*1*–*3*). miRNAs originate from primary transcripts (pri-miRNAs) through sequential cleavage by microprocessor that comprises Dicer-like protein 1 (DCL1), double-stranded RNA (dsRNA) binding protein 1 (DRB1/HYL1) and Serrate (SE) (*4*, *5*). Subsequently, miRNAs are loaded into Argonaute proteins (AGOs) to form RNA-induced silencing complexes (RISCs) that repress gene expression through target cleavage and/or translational repression (*3*). The mode of action of siRNAs is similar to that of miRNAs. However, a prerequisite step for initiating siRNA-mediated RNA silencing in plants is the conversion of single-stranded RNA (ssRNA) substrates to dsRNAs, which is accomplished by RNA-dependent RNA polymerase 6 (RDR6) and suppressor of gene silencing 3 (SGS3) (*6*, *7*). SGS3 functions as a homodimer (*8*) and has been reported to stabilize the primary small RNA (sRNA) cleavage product for dsRNA synthesis (*9*, *10*). In turn, dsRNAs are processed by DCL2 or DCL4 together with its partner DRB4 to 21- to 22-nucleotide (nt) siRNAs, which are eventually loaded into AGO1 to destroy target RNAs (*10*–*12*). As a special situation, inverted-repeat or hairpin PTGS is triggered by self-folded dsRNA from ssRNA substrates that can circumvent the RDR6/SGS3 activity. However, the inverted-repeat/hairpin-derived siRNAs could, in turn, extend beyond the inverted-repeat region to produce secondary siRNAs, and this process entails RDR6/SGS3 function (*13*–*15*). Notwithstanding, the biochemical partners and functional bridges of RDR6/SGS3-DCL4/DRB4 are far less understood compared with microprocessor.

Retinoblastoma-associated protein 48 (RbAp48) functions through multiple epigenetic complexes to affect tumorigenesis, cytoskeletal organization, age-related memory loss, and cardiomyocyte hypertrophy (*16*–*18*). A plant homolog, *FLOWERING LOCUS VE* (*FVE*), has been known to regulate flowering timing and cold response sensitivity (*19*, *20*). Similar to RbAp48, FVE acts as a structural scaffold for the assembly of large complexes exemplified by histone deacetylation and demethylation machinery in epigenetic silencing of protein-coding genes (*21*). In addition, FVE also contributes to transcriptional silencing of transposons such as *AtMu1* and *AtSN1* through RNA-dependent DNA methylation mechanisms (*22*). Despite the well-characterized functions at the epigenetic level, the involvement and mechanistic function of FVE/RbAp48 in PTGS are unclear.

In this study, a new allele of *fve* (*fve-8*) was identified in a forward genetic screen that is compromised in transgene-PTGS pathway. Loss-of-function mutants of *fve* have reduced siRNA production from sense and inverted-repeat transgenes. FVE is localized in the nucleus and cytoplasm, but the cytoplasmic portion of FVE fully rescued the *fve* defect in PTGS. We found that FVE, but not its truncated mutant FVE-8, could interact with SGS3 and promote its homodimerization. Unexpectedly, FVE binds to ssRNAs and dsRNAs with moderate affinities, while FVE-8 shows a significant increase in dsRNA binding activity. These features affect the association and routing of SGS3/RNA to DRB4/DCL2/4 complexes. In turn, FVE promotes DRB4/DCL2/4 activity in generating siRNAs, whereas FVE-8 suppresses the same reaction in vitro. We concluded that FVE synchronizes the RDR6/SGS3-DRB4/DCL2/4 channel to promote siRNA production, whereas FVE-8 hijacks dsRNA substrates to prevent the downstream processing. Thus, this study reveals a noncanonical role of the epigenetic factor FVE in PTGS and sheds light on a new regulatory layer in transgene silencing.

[1]Department of Biochemistry and Biophysics, Texas A&M University, College Station, TX 77843, USA. [2]Research Institute of Resources Insects, Chinese Academy of Forestry, Kunming 650224, China. [3]Department of Horticultural Sciences, Texas A&M University, College Station, TX 77843, USA.
*Corresponding author. Email: xiuren.zhang@tamu.edu
†These authors contributed equally to this work.

RESULTS

A new mutant of attenuated RNA silencing (*ars*) is identified from a forward genetic screen

We previously reported that AGO10 antagonizes AGO1 silencing activity by sequestering miR165/166 to regulate shoot apical meristem development (*23*, *24*). To identify new genes that regulate miR165/166 activity, we designed a reporter system containing a section of genomic *PHABULOSA* (*PHB*) (exon4, intron4, and exon5), which harbors the miR165/166 complementary sequence after splice. The miR165/166 target site is flanked by *Green Fluorescent Protein* (*GFP*) and *Luciferase* (*LUC*) genes and driven by the native *AGO10* promoter (P_{AGO10}-*GFP-PHB-LUC*) (Fig. 1A). The construct was transformed into *Arabidopsis thaliana* Landsberg (Ler) ecotype, and a single-copy homozygous transgenic line (E5-4) with a moderate level of LUC activity was selected for further genetic analysis. To confirm that the defects in miRNA-mediated silencing increase LUC activity, we crossed Ec5-4 (E5-4 introgressed with Col-0 seven times) with *se-2* and *hyl1-2* mutants. Examination of the F_2 population indicated that LUC signal in the mutant backgrounds substantially increased compared with that in wild-type (WT) background, validating the feasibility of the screening strategy (Fig. 1B and fig. S1A). The introgression of Ec5-4 into *rdr6-11* and the *35S-GFP-cPHB-LUC* (*cPHB*, a section containing the exons 4 and 5 of *PHB*) line into *sgs3-1* also markedly increases LUC signal (Fig. 1B and fig. S1A). Since *rdr6* and *sgs3* are two landmark mutants in the transgene PTGS pathway, our dual-reporter system could be exploited to systematically recover genes that are involved in either miRNA or transgene-PTGS pathways.

We performed ethyl methanesulfonate (EMS) mutagenesis on E5-4 seeds. After selfing of EMS-treated plants, 5-day-old M2 seedlings were screened for increased luminescence. In the M2 individuals, several dozen lines were found with increased LUC activity. Since numerous essential mutants recovered in earlier genetic screening for PTGS defects display severe developmental defects, we focused on the lines with no or mild morphological abnormality. Here, we characterized a mutant, named *attenuated RNA silencing 1-1* (*ars1-1*), which displayed a stronger LUC signal than E5-4 (Fig. 1C). RNA blot analysis showed that the *LUC* transcript level in *ars1-1* was four times higher than that in E5-4 (Fig. 1D).

The *ars1-1* mutant was outcrossed with Col-0 to generate F_2 mapping populations. We mapped the mutations to a 1.3-Mb interval on chromosome 2 that harbors eight candidate genes (Fig. 1E and fig. S1B). Complementation experiments with each of eight loci showed that only *At2g19520* (*FVE*) could recover LUC signal to the parental level (fig. S1C). The late-flowering phenotype of the mutant was also fully rescued in the *FVE* complementation lines (Fig. 1C). These results indicated that the mutation in *FVE* is responsible for increased LUC activity in the mutant. The *ars1-1* mutant harbors a G-to-A mutation creating a premature stop codon in the middle of the 12th exon of *At2g19520*, and this mutant was subsequently renamed *fve-8* (Fig. 1F).

FVE plays dual roles in both transcriptional and PTGS pathways

To test whether *fve-8* up-regulates *LUC* expression through a TGS pathway, we first treated *fve-8* with 5-aza-2′-deoxycytidine (aza-dc), a chemical that can abolish DNA cytosine methylation. The transposon element *AtMu1* served as a positive control, as its expression is suppressed by *FVE* at the TGS level (*25*, *26*). *AtMu1* displayed significantly increased expression in *fve-8* compared with E5-4, but this increase was abolished by the aza-dc treatment. However, this scenario was not observed with LUC signal and *LUC* transcripts, inferring that the increased *LUC* expression in *fve-8* may not be through suppression of the TGS pathway (Fig. 2, A and B). We also performed an histone 3 lysine 27 tri-methylation (H3K27me3)–chromatin immunoprecipitation (ChIP) assay with *FLC* and *EF1α* as positive and negative controls, respectively (*27*). We did not observe a noticeable difference of H3K27me3 signal in the *LUC* gene body between *fve-8* and E5-4 lines (Fig. 2C). A marginally reduced H3K27me3 ChIP signal in the *AGO10* promoter and 5′ untranslated region was detected in *fve-8*, suggesting that FVE might have a repressive effect on the expression of endogenous *AGO10* and arguably transgene *LUC* expression at certain levels. This result is in agreement with a previous report that endogenous *AGO10* promoter locus contains relatively lower levels of CHG and CHH (where H is any base except G) DNA methylation in *fve* compared to WT plants (*28*). Notwithstanding, the AGO10 protein level was not affected (fig. S2A), indicating that the enhanced LUC signal in *fve-8* did not result from the possible change of AGO10 ability to decoy miR165/166 (*23*, *24*).

To further investigate whether FVE regulated the *LUC* transgene through TGS, we conducted RNA polymerase II ChIP quantitative reverse transcription polymerase chain reaction (qRT-PCR) assays. We consistently observed that the occupancy of polymerase II at *LUC* gene body was not significantly altered in *fve-8* compared with that of E5-4 (Fig. 2D). Furthermore, we isolated nuclear RNA and quantified the amount of nascent *LUC* transcript. In contrast to *FLC*, RT-PCR analysis did not reveal an obvious difference of *LUC* transcript levels in the nucleus of *fve-8* relative to E5-4 (Fig. 2E). These results further indicated that *fve*-8 does not affect the *LUC* reporter expression through the nuclear TGS pathway.

Because the above results suggested that FVE has an additional non-nuclear function, we examined the subcellular localization of FVE protein. FVE protein not only was highly enriched in the nucleus but also was distributed in the cytoplasm (Fig. 3A and fig. S2C). Computational analysis predicted the presence of a nuclear localization signal (NLS) at the N terminus of FVE (GPKKRGRK) (*19*, *29*). To test ex-nuclear function of FVE, we replaced the FVE NLS with a nuclear export signal (NES; LQLPPLERLTL) (fig. S2B) (*30*) and transfected *35S-YFP-cFVE* (the coding sequence of *FVE*) and *35S-YFP-cFVE*$_{NES}$ constructs into *Nicotiana benthamiana* leaves and *Arabidopsis* protoplasts. The confocal microscopy imaging showed that unlike yellow fluorescent protein (YFP)–FVE, YFP-FVE$_{NES}$ was exclusively accumulated in the cytoplasm (Fig. 3A and fig. S2C). To further validate this result, we generated stable *fve-8;35S–Flag-4Myc (FM)–cFVE* and *fve-8;35S-FM-cFVE*$_{NES}$ transgenic lines. Cell fractionation assays showed that FVE was present in both nucleus and cytoplasm of *fve-8;35S-FM-cFVE* lines, whereas the protein was only detected in the cytoplasm of *fve-8;35S-FM-cFVE*$_{NES}$ lines (fig. S2, D and E). Notably, YFP-FVE amount in the nucleus appeared higher in confocal imaging than in cell fractionation experiments, likely because the florescent signal was concentrated in the nucleus but diluted in the cytoplasm in the confocal imaging. The late-flowering phenotype in *fve-8* was only recovered by *fve-8;35S-FM-cFVE* lines but not *fve-8;35S-FM-cFVE*$_{NES}$ lines despite the fact that FVE protein levels were abundant in the two types of transgenic lines (Fig. 3, B and C). However, both constructs could rescue the LUC signal in *fve-8* to a normal level in E5-4. These results indicated that FVE has separate functions in the nucleus and cytoplasm, and

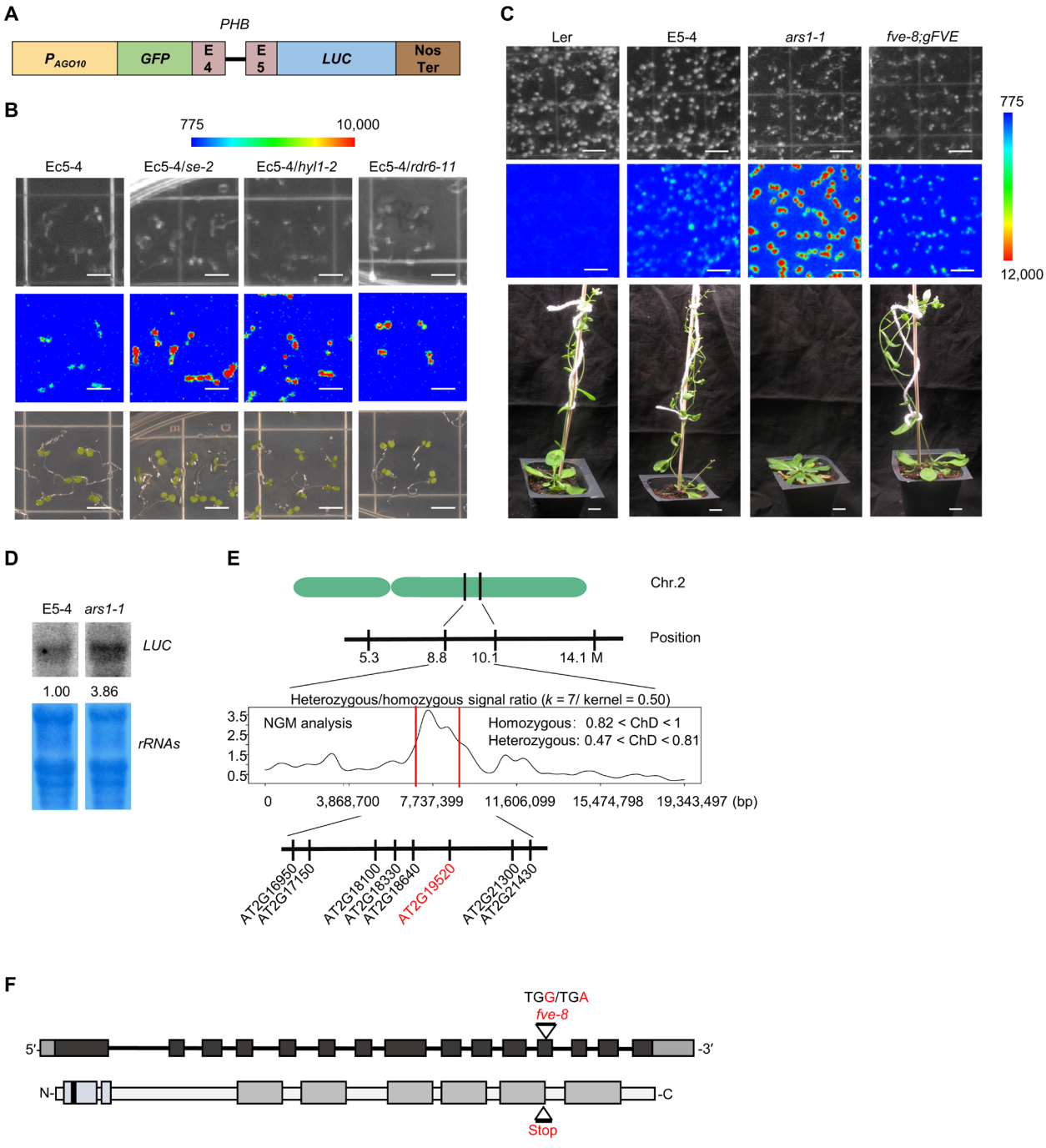

Fig. 1. Isolation of *fve-8* as a new mutant with attenuated RNA silencing through a genetic screening. (**A**) Schematic construct of E5-4 used for the EMS screening in this study. E4 and E5, the fourth and fifth exons of *PHB*, respectively; P_{AGO10}, the native promoter of *AGO10* locus; Nos Ter, nopaline synthase terminator. (**B**) The established mutations in miRNA and siRNA pathways increased LUC luminescence. Five-day seedlings of Ec5-4/*se-2*, Ec5-4/*hyl1-2*, and Ec5-4/*rdr6-11* were photographed in bright field (top), under charge-coupled device (CCD) camera for LUC signal (middle), and under regular camera (bottom). The crossing lines of M17-1 with *sgs3-1* displayed similar patterns (see also fig. S1A). Scale bars, 0.5 cm. (**C**) Mutation in *FVE* caused increased LUC luminescence. Five-day seedlings of *ars1-1* (*fve-8*), E5-4, and *fve-8; gFVE* were photographed in bright field (top) and under CCD camera for LUC signal (middle). The signals were displayed by LightField software. Scale bars, 1 cm. Bottom: Six-week-old *ars1-1/fve-8* and complementation lines displayed later and normal flowering phenotypes, respectively. Scale bars, 1 cm. (**D**) RNA blot analysis showed *LUC* transcript accumulated in *ars1-1*(*fve-8*) and E5-4. Ribosomal RNA is control. (**E**) Next-generation mapping (NGM) analysis of F_2 mapping population delineated eight candidates in 1.3 Mb of chromosome 2. bp, base pairs. (**F**) Top: The gene structure of *FVE* includes untranslated regions (gray boxes), exons (black boxes), and introns (lines). The *fve-8* mutation (triangle) is labeled. Bottom: The protein schematic shows a low complexity region (light gray boxes), 6 × WD40 domains (dark gray boxes), and putative nuclear localization signal (NLS; black box).

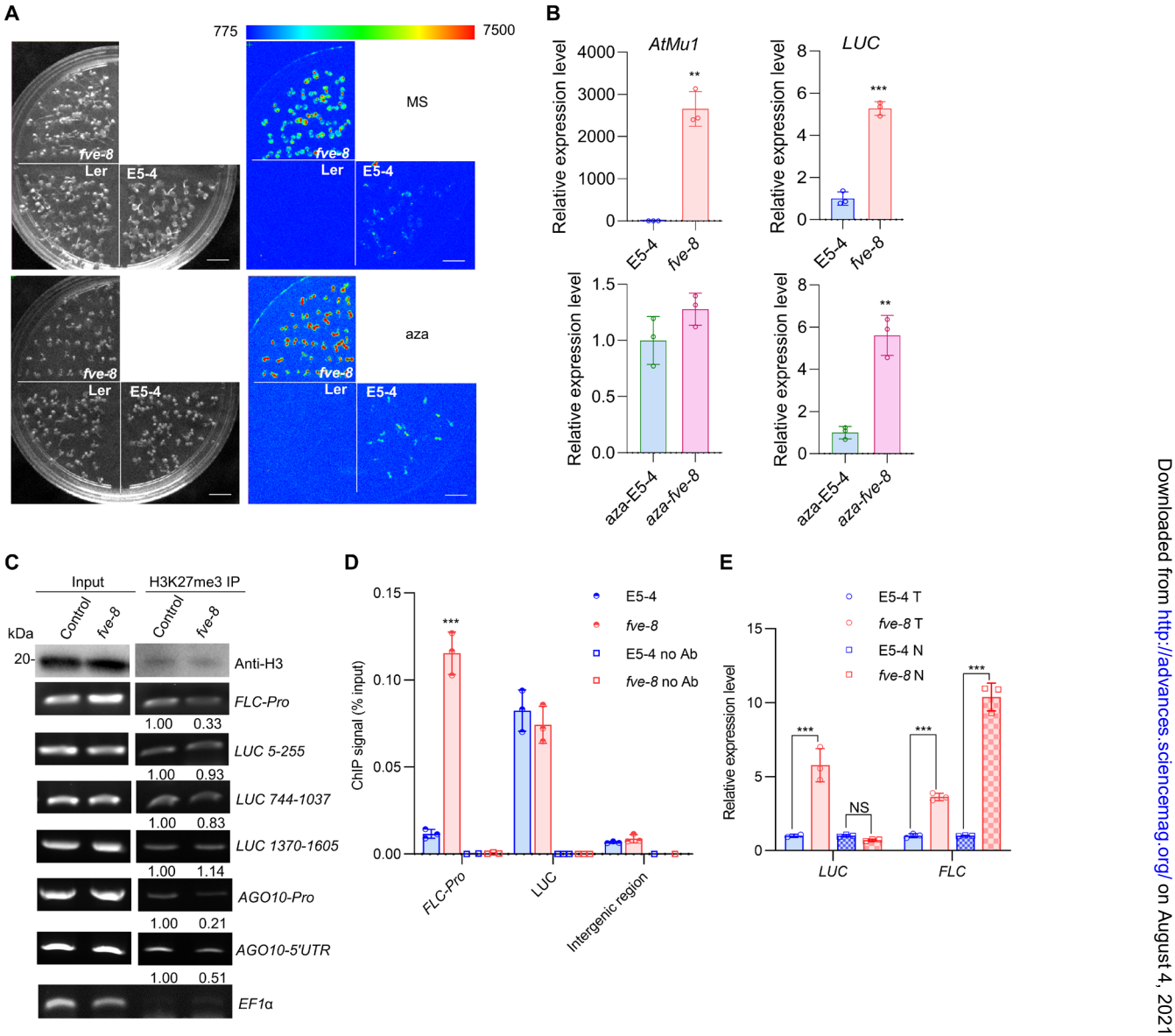

Fig. 2. *FVE* does not regulate *LUC* expression through the TGS pathway. (**A**) 5-azacytidine-2′-deoxycytidine (aza-dc) treatment did not alter the patterns of LUC luminescence in *fve-8* and E5-4 compared with mock. Five-day-old seedlings were photographed, respectively. Scale bars, 2 cm. (**B**) qRT-PCR of *LUC* and *AtMu1* transcripts in materials collected from (A). *EF-1α* is an internal control. The asterisks indicate a significant difference between mutants and E5-4 with ±SD ($n = 3$) biologically independent replicates. *$P < 0.01$; ***$P < 0.001$; *t*-test. (**C**) ChIP-PCR assay did not show obvious change of H3K27me3 mark in *LUC* transgene locus of *fve-8* and E5-4 control. Western blot assay using an anti–histone 3 (H3) antibody validated the IP enrichment of H3K27me3. The membrane image was split because of different intensities of the signal. Promoter of *FLC* (P_{FLC}) and *EF-1α* were amplified as positive and negative controls, respectively. (**D**) ChIP–qRT-PCR assay did not reveal significant change of polymerase II occupancy in *LUC* locus in *fve-8* and E5-4. P_{FLC} serves as a positive control. ChIP without the antibody (no Ab) serves as negative controls. The data were presented as means ± SD ($n = 3$) biologically independent replicates. **$P < 0.001$; *t*-test. (**E**) qRT-PCR did not reveal significant difference of the nascent *LUC* transcript level in the nuclear fraction of *fve*-8 compared with that of E5-4. The data normalization is similar to (B). ***$P < 0.001$; *t*-test. T, total RNA; N, RNA from nuclei; NS, not significant.

there must be a new function of FVE_{NES} in cytoplasmic RNA silencing. To further validate this concept, we also generated *FVE* native promoter–driven complementation lines (*fve-8;* P_{FVE}*-cFVE* and *fve-8;* P_{FVE}*-cFVE*$_{NES}$) and determined LUC luminescence in parallel. Again, a majority of transformants of the two constructs could recover the LUC signal in *fve-8* to the level in E5-4 (Fig. 3D). In agreement with the changes of the LUC signal, *LUC* transcripts were significantly reduced in the two kinds of complementation lines (Fig. 3E). This result indicated that cytoplasmic FVE is functionally sufficient to silence *LUC* transgene. Notably, we observed that *LUC* expression was marginally reduced in *fve-8;* P_{FVE}*-cFVE*$_{NES}$ compared with that in *fve-8;* P_{FVE}*-cFVE*, which was likely due to variations of FVE expression in independent lines (Fig. 3E).

To test whether FVE_{NES} had a similar impact on endogenous *AGO10*, we examined the expression of *AGO10*, the assumed proxy of the *LUC* transgene at an epigenetic status. The *AGO10* level was approximately twofold higher in *fve-8* when compared with E5-4 and was fully rescued in *fve-8;* P_{FVE}*-cFVE*. However, the *AGO10*

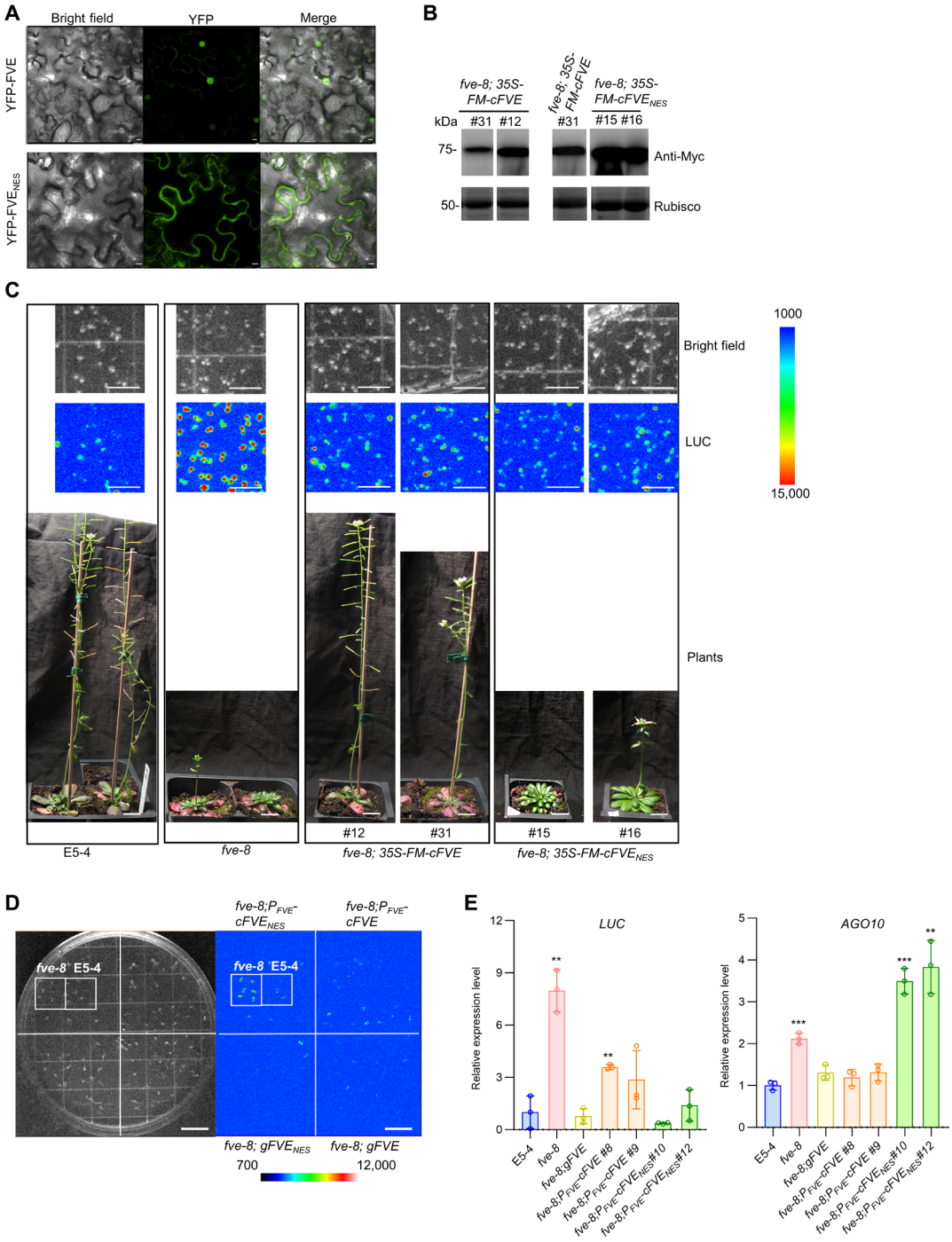

Fig. 3. *FVE* regulates *LUC* expression through a PTGS pathway. (**A**) Confocal microscope imaging showed subcellular localizations of YFP-FVE and YFP-FVE$_{NES}$. The proteins were expressed in leaves of *N. benthamiana*. Scale bars, 50 μm. (**B**) Western blot analysis of FM-cFVE and FM-cFVE$_{NES}$ accumulation in overexpression lines using an anti-Myc antibody. Coomassie brilliant blue (CBB)–stained ribulose-1,5-bisphosphate carboxylase-oxygenase (rubisco) is an internal control. (**C**) FVE$_{NES}$, different from FVE, could efficiently rescue LUC luminescence but not the late-flowering phenotype of *fve-8* to the parental level. Five-day-old seedlings in (B) were photographed in bright field (top) and under CCD camera for LUC signal (middle). Scale bars, 1 cm. The signals were displayed by LightField software. Bottom: Six-week-old plants were photographed. Scale bars, 1 cm. (**D**) FVE$_{NES}$ could efficiently rescue LUC luminescence in *fve-8* to the parental level. Five-day-old seedlings or T_1 transformants of the indicated constructs were photographed under CCD camera. Scale bars, 2 cm. (**E**) qRT-PCR analysis showed that *LUC* transgene and endogenous *AGO10* were regulated differently by *FVE* and *FVE$_{NES}$*. Five-day-old seedlings of *fve-8*, E5-4, and indicated transgene lines were used for the assay. *EF-1α* is an internal control. The asterisks indicate significant difference between the mutants and E5-4 with ±SD ($n = 3$) biologically independent replicates. $^{**}P < 0.01$; $^{***}P < 0.001$; *t*-test.

level was increased approximately three- or fourfold in *fve-8; P_{FVE}-cFVE$_{NES}$* transformants (Fig. 3E). These results indicated that the nuclear-localized FVE, but not the cytoplasmic FVE, repressed the transcription of *AGO10*, but not that of *LUC* transgene at an epigenetic level. This observation also suggested that the slightly reduced H3K27me3 mark in *fve-8* would be likely from the promoter of endogenous *AGO10* rather than the one for *LUC* transgene (Fig. 2C). This result further suggested that FVE affects native genes and transgenes differently at the epigenetic level. One plausible hypothesis for the enhanced *AGO10* expression in the *FVE$_{NES}$* complementation lines is that FVE$_{NES}$ might hijack nuclear FVE cofactors from the nucleus to the cytoplasm and thereby partially releasing the epigenetic suppression at the native *AGO10* promoter. Together, we concluded that FVE has a noncanonical role in regulating *LUC* expression at a PTGS level in the cytoplasm, in addition to its classic roles in epigenetic regulation of native genes in the nucleus.

fve-8 has a negligible impact on biogenesis of endogenous sRNAs

Given that cytoplasmic FVE could promote PTGS, we evaluated the impact of *fve* mutations on the miRNA and trans-acting siRNA (ta-siRNA) pathways. sRNA sequencing (sRNA-seq) did not reveal significant changes in the accumulation of most miRNAs and ta-siRNAs in *fve-8* compared with E5-4 plants (Fig. 4A). The results were conclusively validated by sRNA blot assays (Fig. 4, B and C). Similarly, there were no significant changes in the accumulation levels of most pri-miRNAs (Fig. 4D) and miRNA targets (Fig. 4E).

We next examined whether the attenuated LUC signal was due to miR166-mediated translation repression. Isogenic *fve-8* (−/−) and heterozygous (+/−) lines containing *35S-PHB-Myc*, *35S-PHBm-Myc*, or *$P_{MIR166b}$-CNA-Myc* were generated. The accumulation of transgenic proteins was similar between *fve-8* (−/−) and *fve-8* (+/−) (Fig. 4F). These results indicated that the enhanced LUC signal in *fve* did not result from defects of miR165/166 activity. In addition, the expression levels of key components in miRNA and RNA decay pathways were not affected except for noticeable increases in *XRN2* and *ESP3* levels (fig. S3, A and B). Thus, it is unlikely that LUC activity in *fve-8* was caused by indirect effect on the miRNA and RNA decay pathways.

FVE promotes the accumulation of transgene-derived siRNA

We investigated whether *fve-8* affects the transgene-PTGS pathway. In the sRNA-seq dataset, we found that the 21- to 22-nt sRNAs derived from *GFP-PHB-LUC* transgene were clearly reduced in *fve-8* compared with E5-4 (Fig. 5, A and B). This result suggested that FVE decreases *LUC* accumulation through regulating transgene-derived siRNAs. To further test this, we crossed *fve-8* with L1 line, which is an established model system for a sense transgene-PTGS pathway with a silenced β-glucuronidase (*GUS*) transgene reporter (*7*). Genotyping was performed for the F_2 population with a pair of derived cleaved amplified polymorphic sequences (dCAPS) primers designed to distinguish *fve-8* from WT *FVE* (Fig. 5C). An sRNA blot showed that the amount of 21/22-nt-*GUS* loci-derived siRNAs in *fve-8* (−/−) decreased compared with that in heterozygotes (+/−) or WT background (+/+) (Fig. 5D). Consistently, GUS activity was higher in *fve-8* (−/−) than that in *fve-8* heterozygotes (+/−) or WT (+/+) lines (Fig. 5E). Thus, these results indicated that FVE is indeed engaged in the transgene-PTGS pathway.

To test whether *FVE* affects the silencing triggered by inverted-repeat transgene, we used CRISPR-Cas9 technology to knock out *FVE* in a well-known *hpCHS* (hairpin *chalcone synthase*) reporter line that lacks flavonoid pigments due to the silencing of *CHS* (Fig. 5F) (*31*). At least two biallelic homozygous mutants were obtained (Fig. 5G). The *CHS* siRNA level in the cas9-*fve* background was remarkably lower than that in *FVE* (+/+) background (Fig. 5H and fig. S3C). Correspondingly, the leaf color of *cas9-fve* mutants became darker than that of the parental line due to the release of the silenced *CHS* (Fig. 5I). Similarly, the seed coat of *cas9-fve* mutants turned brown, indicative of flavonoid production, whereas the parental line produced light yellow seed coat pigmentation (Fig. 5I). Both leaf and seed phenotypes indicated that the endogenous *CHS* expression level was increased in the *fve* mutants compared with the parental line.

In conclusion, FVE participates in the silencing pathway triggered by both sense and inverted-repeat transgenes and reduces transgene siRNA production. One possibility for recovering the *fve* mutant using the miRNA-targeted readout is likely because the transgene construct harbors a large section of foreign transgenes (*GFP-LUC*) that is highly sensitive to transgene silencing. Another likely reason is that we focused on the mutants with relatively normal morphology and avoided the lines with severe developmental defects (i.e., *ago1*, *hyl1*, and *se*-like mutants), which are often controlled through the miRNA pathway.

FVE interacts with SGS3 and promotes its homodimerization

Next, we hypothesized that FVE might target key components in the transgene-PTGS pathway. To test this, we conducted a yeast two-hybrid (Y2H) screening of more than a dozen candidates involved in RNA silencing (Fig. 6A and fig. S4A). We found that FVE specifically interacted with SGS3. We then tested several truncated forms of SGS3 with the N-terminal region, the zinc finger (ZF) domain, the rice gene X and SGS3 (XS) domain, and the coiled-coil (CC) domain. Y2H assays showed that FVE interacted with 219 to 450 amino acid residues of SGS3, which harbors the ZF and XS domains (fig. S4B). To further validate the FVE-SGS3 interaction, we conducted Co-IP assays using *fve-8; P_{FVE}-FM-gFVE* transgenic lines. We immunopurified FVE complexes using an anti-Flag antibody and readily recovered SGS3 protein in the immunoprecipitates. The addition of ribonuclease A (RNase A) did not disrupt the interaction of FVE and SGS3, indicating that their interaction is RNA independent (Fig. 6B). We also conducted bimolecular fluorescence complementation (BiFC) and LUC complementation imaging (LCI) assays (Fig. 6C and fig. S4C). For the BiFC, we cotransfected N-terminal fragment of YFP (nYFP)-FVE and C-terminal fragment of YFP (cYFP)-SGS3 into *Arabidopsis* protoplasts with nYFP-SGS3 and cYFP-SGS3 as a positive control. Again, we observed YFP fluorescence complementation between FVE and SGS3, but not for other combinations (Fig. 6C). In the LCI, FVE displayed LUC complementation with SGS3, as did the positive control of AGO1 and *cucumber mosaic virus* (CMV) 2b (*32*), but to a lesser extent (fig. S4C). Collectively, these results indicated that FVE interacts with SGS3 and is targeted to the cytoplasmic granules. FVE-8, a truncated form of FVE encoding the N-terminal 413 amino acid residues and missing the last two WD40 (trp-asp dipeptide) domains (FVE$_{5+6}$), lost its interaction with SGS3 (Fig. 6A), suggesting that only a full-length FVE can interact with SGS3. We also noticed that FVE is monomeric, whereas FVE-8 could form a dimer or oligomer (Fig. 6A). Furthermore, FVE-8 could not interact with FVE (Fig. 6A), suggesting that the C-terminal part of FVE might harbor an autoinhibitory domain, preventing self-interaction under normal conditions.

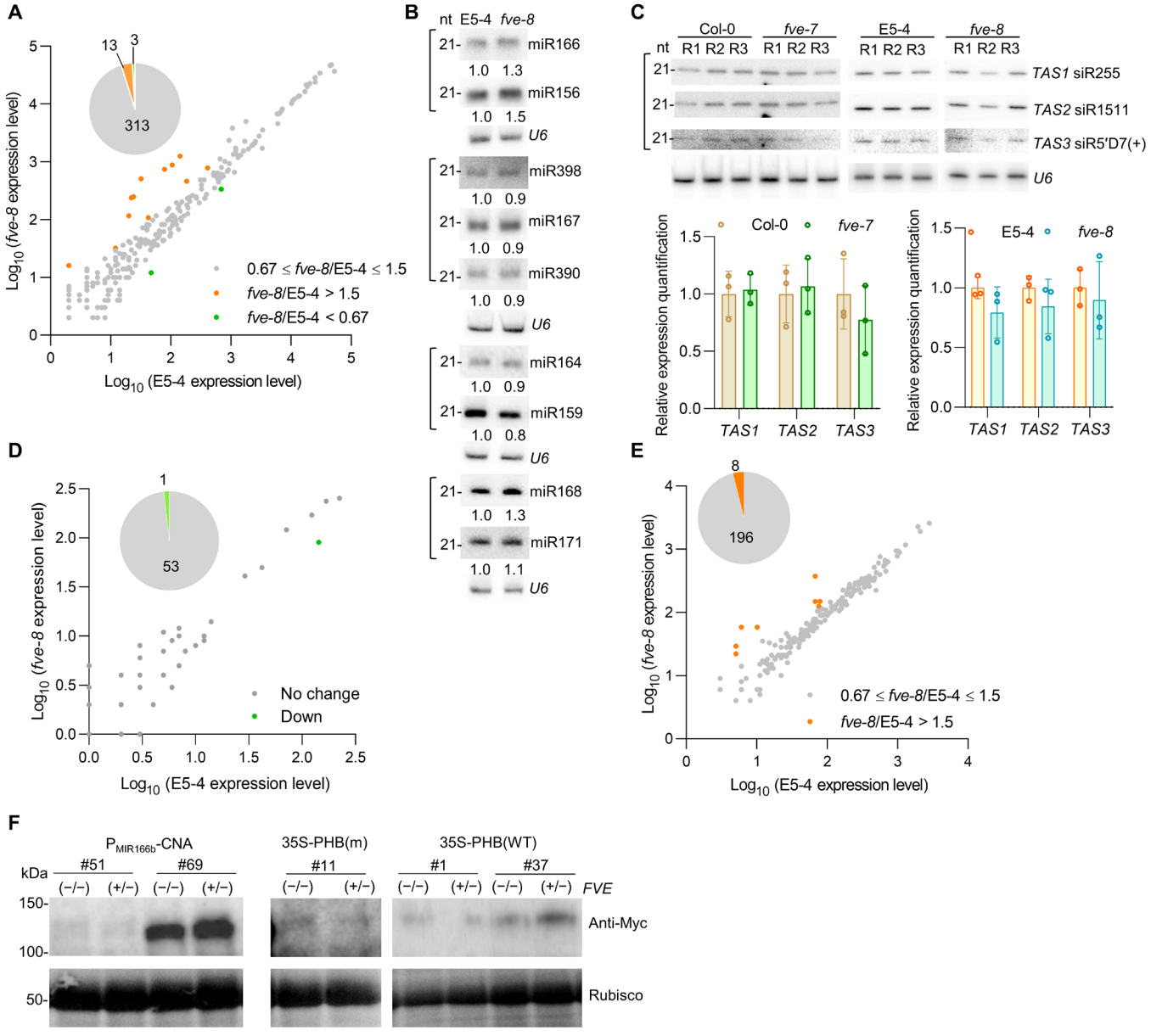

Fig. 4. *FVE* has a negligible impact on the endogenous PTGS pathway. (**A**) sRNA-seq analysis showed sRNA distributions in *fve-8* and E5-4 with relatively stable (0.67 ≤ *fve-8*/E5-4 ≤ 1.5, gray), increased (*fve-8*/E5-4 > 1.5, orange), and decreased (*fve-8*/E5-4 < 0.67, green) expression. The *x* and *y* axes indicate the logarithms of normalized expression levels of sRNAs. The top-left pie in the top left indicates the numbers of different categories of sRNAs. See also table. S2. (**B** and **C**) sRNA blot analyses of selected miRNAs (B) and ta-siRNAs (C) in the *fve* mutants and WT plants. *U6* is a control. In (B) and (C), the experiments were independently repeated with similar results. In (C), statistics of three replicates (R) was shown at the bottom. (**D** and **E**) RNA-seq analysis showed that the expression of most of *MIR* genes (D) and sRNA target genes (E) was not affected in *fve-8*. The *x* and *y* axes indicate the logarithms of the normalized gene expression levels in E5-4 and *fve-8*, respectively. The pie in the top left indicates the numbers of different categories of *MIR* genes (D) and sRNA target genes (E). See also table. S2. (**F**) Western blot analyses showed that protein levels of several miRNA targets were not changed in F_2 of segregated *FVE* (+/) and *FVE* (−/−) using an anti-Myc antibody. CBB staining of rubisco is a control.

We examined whether the *fve-8* mutation altered SGS3 protein levels, but this possibility was disproved by Western blots (fig. S4D). Next, we investigated whether *fve-8* affected SGS3 cellular compartmentation. The *35S*-driven YFP-SGS3 accumulated in granule-like foci in the transfected protoplasts of *fve-8*, E5-4, and *fve-8; gFVE* lines (fig. S5, A and B), reminiscent of the SGS3 foci reported previously (*8*, *33*). The numbers of foci per cell were comparable in those lines, indicating that the *fve-8* mutation might not change the cellular localization of SGS3 (fig. S5A). However, a BiFC assay for SGS3 homodimerization (*8*) revealed that the number of foci for SGS3 homodimers per protoplast was significantly reduced in *fve-8* compared with either E5-4 or *fve-8; gFVE* (Fig. 6D). These results indicated that *fve-8* affects SGS3 homodimerization and, consequently, SGS3-mediated function in vivo. To further investigate this, we performed yeast three-hybrid (Y3H) and evaluated the growth rate of transfected colonies as a proxy of SGS3-SGS3 homodimer level. In

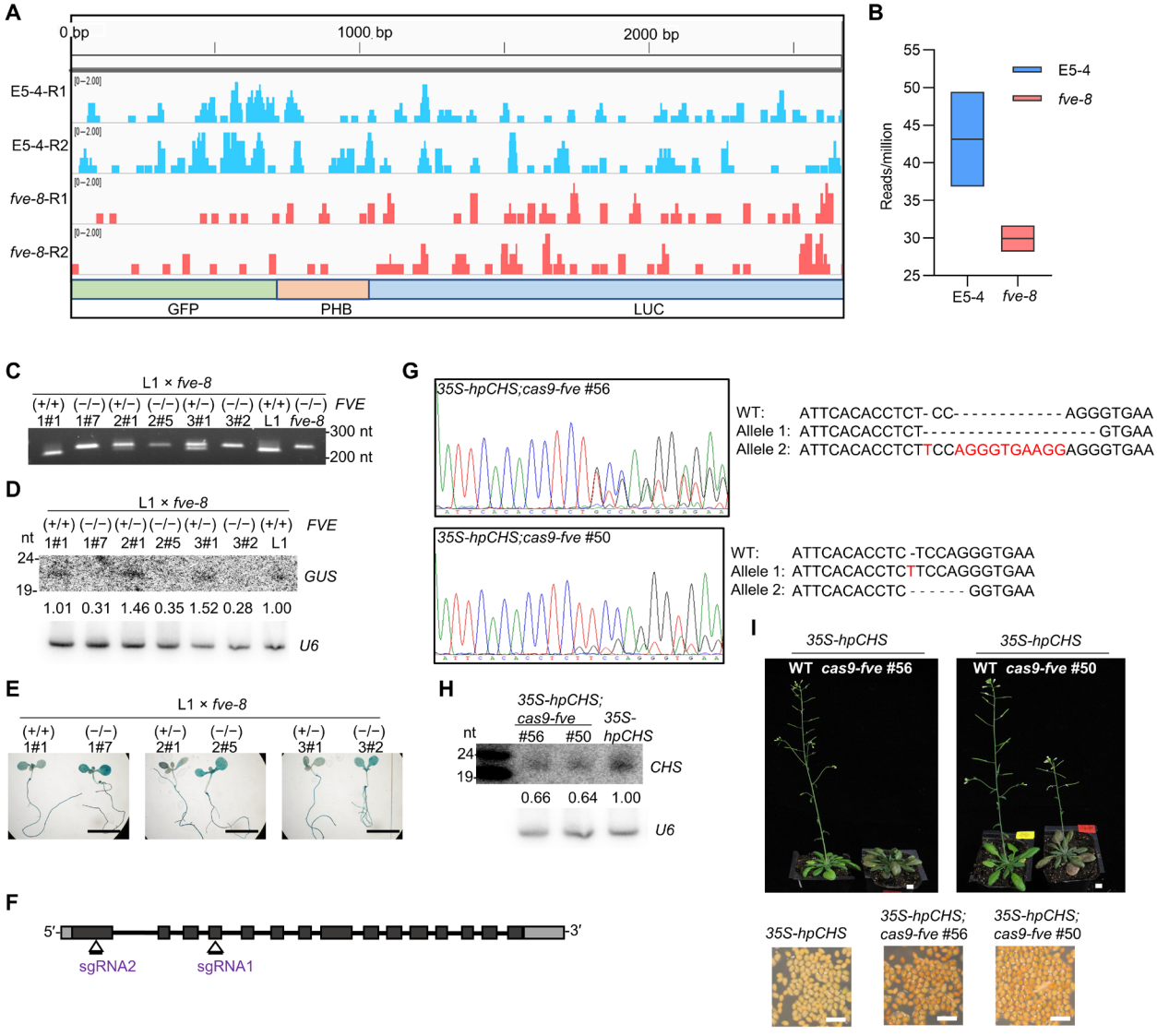

Fig. 5. Transgene-derived siRNA is decreased in *fve-8* compared to WT. (**A**) The Integrative Genomics Viewer (IGV) graphs showed the reads distribution of 21- to 22-nt sRNAs in the *GFP-PHB-LUC* gene body. Two independent biological repeats were sequenced for each material. (**B**) Box plot showed reduced 21- to 22-nt siRNA (reads per million) mapped to the *GFP-PHB-LUC* in *fve-8*. Lines in the middle of boxes indicate mean values from two replicates. (**C**) Genotyping of different lines of L1 × *fve-8* F_2 materials by PCR with dCAPS primers, followed by digestion by Bam HI. (**D**) sRNA blot assay of *GUS*-mapped siRNAs in 10-day-old F_2 seedlings genotyped in (C). *U6* is a loading control. This assay was performed with three groups of isolated *FVE* (+/) and *FVE* (−/−) F_2 materials. (**E**) GUS staining assay with 10-day-old seedlings analyzed in (D). Scale bars, 1 cm. At least three independent crossed lines were tested and showed similar results. (**F**) Diagram shows the guide RNA–targeted sites in *FVE* transcript using the CRISPR-Cas9 system. (**G**) Sequence results of two independent *35S-hpCHS; cas9-fve* mutants. The edited DNA sequences were shown. Dashes in alleles and red nucleotides indicate deletion and insertion, respectively. (**H**) sRNA blot assay showed that transgenic *CHS*-mapped siRNAs were reduced in the *fve* mutants in F_2 plants genotyped in (G). *U6* is a loading control. Three biological repeats were conducted with similar results (see also fig. S3C). (**I**) *CHS* loss-of-function specific color phenotypes of 45-day-old plants (top) and seeds (bottom) from the lines used in (H). Scale bars, 0.2 cm.

this system, the addition of methionine is used to suppress *FVE* expression driven by a promoter *Met23*. We observed that the inclusion of FVE could promote colony growth in the combinations of SGS3-FVE-SGS3 relative to SGS3-SGS3 in the absence of methionine. However, the addition of methionine eliminated the growth advantage of the SGS3-FVE-SGS3 cells (Fig. 6E and fig. S5C). This result further validated that FVE could facilitate SGS3-SGS3 homodimerization. This conclusion is also supported by the in vitro pull-down assay in which the application of FVE [but not FVE-8 or small ubiquitin-like modifier (SUMO) protein] enhanced the interaction between maltose binding protein (MBP)–SGS3 and glutathione *S*-transferase (GST)–SGS3 (Fig. 6F and fig. S5D).

FVE does not affect RDR6 activity in vitro

SGS3 and RDR6 interact in specific cytoplasmic granules and form SGS3/RDR6 bodies (*33*). To investigate whether FVE influences polymerase activity of RDR6, we used recombinant RDR6, SGS3, FVE, and FVE-8 from either *Escherichia coli* or a baculovirus-insect

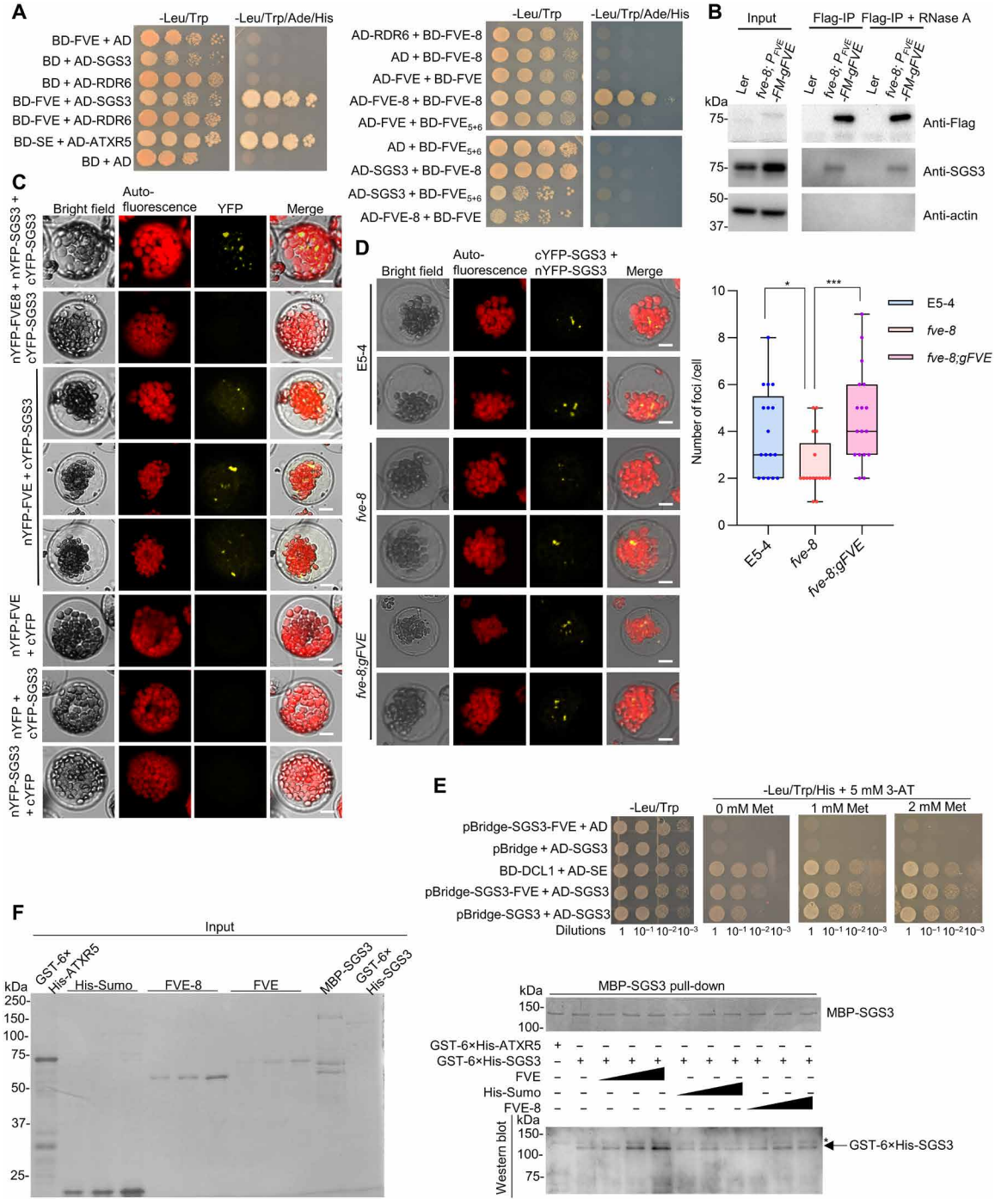

Fig. 6. FVE interacts with SGS3 and promotes its homodimerization. (**A**) Y2H screening showed the FVE-SGS3 interaction. SE and ARABIDOPSIS TRITHORAX-RELATED PROTEIN 5 (ATXR5) were used as positive control. AD, galactose-responsive transcription factor (GAL4) activation domain; BD, DNA binding domain; FVE_{5+6}, truncated FVE with WD40 domains #5 and #6. (**B**) Co-IP validated the FVE-SGS3 interaction. IP was performed with an anti-Flag antibody. Western blot assay was performed with the indicated antibodies. The experiment was independently repeated with similar results. (**C**) Confocal imaging showed the interaction between FVE and SGS3. cYFP and nYFP without fusion proteins serve as negative controls. nYFP-SGS3 and cYFP-SGS3 serve as a positive control. Scale bars, 10 μm. (**D**) BiFC of YFP assays showed that FVE promotes homodimerization of SGS3. Box plot showed numbers of SGS3 dimer foci per cell. The line in the middle of the box refers to the median. The whiskers are drawn from minimum to maximum percentiles. Individual data points are shown. *$P < 0.05$; ***$P < 0.001$; *t*-test. (**E**) Y3H assay showed that FVE promoted the interaction between pBridge-SGS3 and AD-SGS3. The colonies of pBridge-SGS3-FVE-AD-SGS3, but not those of pBridge-SGS3-AD-SGS3, grew in the dilution of 10^{-2} without Met. SE and DCL1 serve as positive control. See also fig. S5B and Materials and Methods. (**F**) In vitro pull-down assay showed that FVE promoted SGS3 homodimerization. GST-ATXR5, His-SUMO, and FVE-8 serve as negative controls. Left: Input. Top right: Bead-recovered MBP-SGS3 by CBB staining. Bottom right: Western blot analysis using an anti-GST antibody (see also fig. S5C).

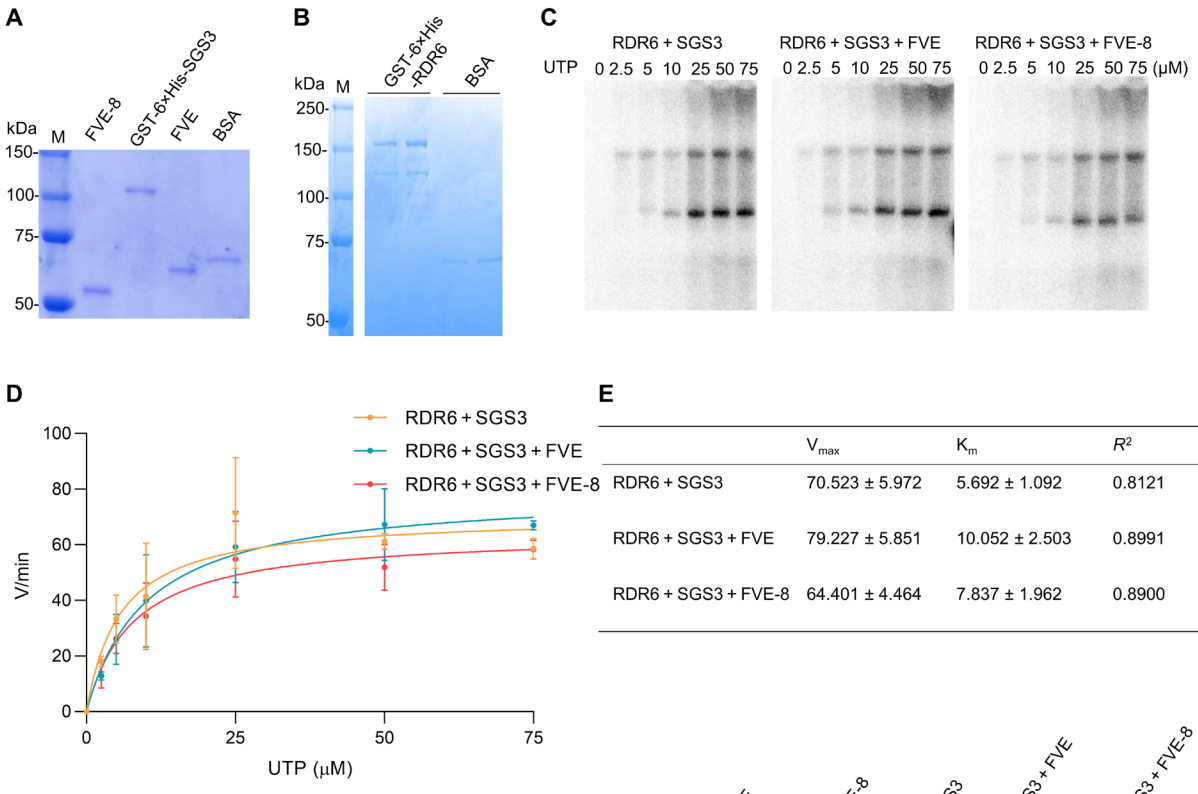

E

	V_{max}	K_m	R^2
RDR6 + SGS3	70.523 ± 5.972	5.692 ± 1.092	0.8121
RDR6 + SGS3 + FVE	79.227 ± 5.851	10.052 ± 2.503	0.8991
RDR6 + SGS3 + FVE-8	64.401 ± 4.464	7.837 ± 1.962	0.8900

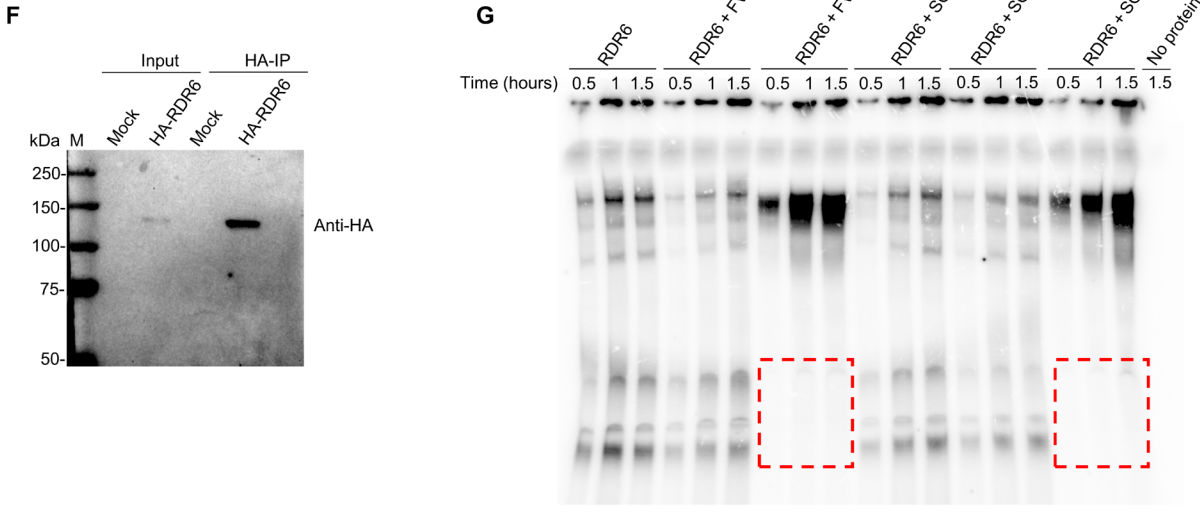

Fig. 7. In vitro reconstitution assays showed that FVE might not have significant enhancement effect on RDR6/SGS3 activity in vitro. (**A** and **B**) SDS-PAGE of purified recombinant proteins FVE-8, GST-6×His-SGS3, FVE (A), and GST-6×His-RDR6 (B). Bovine serum albumin (BSA) is a reference. (**C**) In vitro assays of RDR6 activity with different combinations of proteins. The reaction took place in 20 min with a range of [^{32}P]-UTP dosage. At least three independent repeats were conducted with similar results. Signals were detected by phosphor imaging. (**D**) Michaelis-Menten model of RDR6 reaction velocity calculated from (C). The velocity was calculated from image quantification of (C) with ±SD ($n = 3$). Individual data points were shown. (**E**) V_{max}, K_m, and R^2 values calculated with (D). (**F**) Western blot analysis of immunoprecipitated HA-tagged RDR6 prepared from *N. benthamiana* using an anti-HA antibody with mock treatment as a negative control. (**G**) Semi in vitro assays of RDR6 activity in a time course with ssRNA substrate. HA-RDR6 was incubated with and without different combinations of proteins for the indicated time points. Signals were detected by phosphor imaging. Note that sRNA products otherwise in red dashed squares in the FVE-8–treated reactions were shifted up compared with those in other reactions.

cell system and established an in vitro RDR6/SGS3 reconstitution system (Fig. 7, A and B). After the reaction, the samples were digested with proteinase K and then vigorously washed by phenol and chloroform before fractionation in a urea–polyacrylamide gel electrophoresis (PAGE) gel. Michaelis-Menten kinetics analysis showed that the RDR6/SGS3 activity was not significantly affected by FVE. In contrast, FVE-8 appears to have some marginally inhibitory effect on the RDR6/SGS3 activity in vitro (Fig. 7, C to E). We next hypothesized that the RDR6/SGS3 complex entails some endogenous cellular cofactors for optimized function. To test this, we immunoprecipitated

hemagglutinin (HA)–tagged RDR6 using *N. benthamiana* based on previous reports (Fig. 7F) (*34*, *35*) and reconducted the assay. This time, the samples were directly denatured and fractionated in the urea-PAGE without prior protein digestion. Again, we did not observe an enhanced effect of FVE on RDR6/SGS3 performance in vitro (Fig. 7G). Unexpectedly, an unusually strong signal was detected in the reaction mixture containing FVE-8 but no other proteins. A closer examination of the urea-PAGE gel revealed that the shorter RNA products disappeared in the FVE-8–containing reaction (Fig. 7G), suggesting that FVE-8 might retain RNA transcripts produced by RDR6/SGS3.

FVE and FVE-8 bind to RNA

To further determine whether FVE and FVE-8 associated with RNA in vitro, we performed electrophoretic mobility shift assays (EMSAs). EMSAs showed that FVE could bind to ssRNA with a disassociation constant (K_d) of 145.5 ± 13.5 nM (Fig. 8, A and B, and fig. S6, A and B). FVE could also bind to dsRNA with an apparent K_d of 143.5 ± 4.0 nM (Fig. 8, C and D, and fig. S7, A and B). These results were unexpected, as RbAp48 has not been previously reported to bind to RNA. To further confirm this observation, we performed ribonucleoprotein IP (RIP) experiments in which we cotransfected *35S-FM-FVE* with *35S-LUC* or *35S-hpLUC* constructs in *N. benthamiana*, respectively. The RIP result showed that *LUC* transcript was recovered in the FVE immunoprecipitates, but not in the control, suggesting that FVE is indeed an RNA binding protein in vivo (Fig. 8E).

Similar to FVE, FVE-8 bound to ssRNA with a moderate binding affinity (K_d = 149.3 ± 76.0 nM) (Fig. 8, F and G, and fig. S6, C and D). Different from a single-shifting band of FVE-ssRNA binding, there were two shifting bands of FVE-8–ssRNA in the EMSA, which is reminiscent of the association of dimerized HYL1 with RNA (*5*). FVE-8 displayed a substantially increased binding affinity to dsRNA with an apparent dissociation constant appK_d = 5.3 ± 0.3 nM and h = 1.997 (Fig. 8, H and I, and fig. S7, C and D). The h value and the sigmoidal FVE-8–dsRNA binding curves suggested cooperativity between multiple nucleic acid binding sites in FVE-8 in substrate binding. This result was consistent with the fact that FVE-8 could form dimer or oligomers in vitro and in vivo.

A previous study showed that SGS3 bound to dsRNA but not ssRNA (*36*). We revisited this assay and found that SGS3 could indeed bind to dsRNA with a binding affinity of appK_d = 30.8 ± 1.4 nM (Fig. 8, J and K, and fig. S7, E and F). For ssRNA binding, SGS3 showed a complicated scenario. A subtle shift was observed, but the bound ribonucleoprotein complexes were quickly disassociated and could not reach a complete shift (Fig. 8L and fig. S6, E and F), suggesting that SGS3 has a very low binding affinity for ssRNA.

Given that FVE interacts with SGS3, we examined whether these constituents could synergistically cooperate in binding to RNA. EMSAs showed that coincubation of FVE and SGS3 with ssRNA resulted in a shifting pattern different from the mobility of either FVE-ssRNA or SGS3-ssRNA complexes (Fig. 8M and fig. S6, G and H). These results suggested that FVE-SGS3-ssRNA can form a new stable complex with distinct electrophoretic mobility. In contrast, coincubation of FVE-8 and SGS3 with ssRNA displayed a similar mobility-shifting pattern to those of either SGS3-ssRNA or FVE-8–ssRNA complexes (Fig. 8M and fig. S6, G and H). Notably, the addition of FVE-8 to FVE-ssRNA or FVE-SGS3-ssRNA complex did not alter the mobility shift patterns. These results suggested that FVE (but not FVE-8) could promote SGS3-ssRNA binding and further implicate that FVE could facilitate and strengthen SGS3 association to the transgene transcripts to produce dsRNA substrates in vivo.

For the binding to dsRNA, FVE and SGS3 appeared to be in the same ribonucleoprotein complex. However, regardless of which protein was coincubated with FVE-8, the shifting pattern of the mobility was always identical to that of FVE-8–dsRNA alone, which clearly relates to its predominant strong affinity to dsRNA compared with other proteins (Fig. 8N and fig. S7G). Although the differential RNA binding patterns by the combinations of the proteins above do not appear to affect dsRNA synthesis in the RDR6/SGS3 assays in vitro, they likely affect their function in vivo and the downstream step of siRNA synthesis.

FVE promotes while FVE-8 impedes DCL2/4 activity in vitro

The dsRNA produced by RDR6/SGS3 are routed to DRB4/DCL2/4 complexes for further processing. DRB4 serves as an auxiliary factor of DCL4 (*37*), similar to DRB1 with DCL1 in producing miRNAs (*4*, *5*). Given that FVE could interact with DRB2, we next hypothesized that FVE might interact with DRB4, a homolog of DRB2 (*38*), to regulate DRB4/DCL2/4 activity. Both FVE and FVE-8 showed interaction with DRB4 in the LCI assay (Fig. 9A and fig. S8A). The interaction between FVE and DRB4 was further confirmed by the Co-IP assay with protein extracts from transfected *N. benthamiana* leaves (Fig. 9B) (*39*). Y2H and LCI assays for SGS3 and DRB4 also detected their interaction in vivo (Fig. 9, C and D, and fig. S8B), which suggested that the FVE/SGS3/dsRNA ribonucleoprotein complex could be channeled to DRB4/DCL2/4 machinery through FVE/SGS3/DRB4 interaction. This result is consistent with the previously reported partial colocalization of SGS3 with DCL4 complexes (*40*).

Last, we investigated the impact of FVE and FVE-8 on DRB4/DCL2/4 activity. 3HA-DCL2 and 3HA-DCL4 were immunoprecipitated from *N. benthamiana* leaves that were transfected with corresponding constructs, respectively (fig. S8, C and D). DRB4 was purified from *E. coli* (fig. S8E). We performed in vitro DCL2/4 assays by incubating IP products and dsRNA substrates with different combinations of FVE or FVE-8. The incubation with FVE consistently enhanced the DCL2 and DCL4 activity, while the incubation with FVE-8 remarkably quenched the activities of DCLs (Fig. 9, E to H, and fig. S8, F and G). Our results suggested that FVE could promote DCL4 activity likely through interaction with DRB4, whereas FVE-8 hijacked dsRNA and inhibited its processing despite its interaction with DRB4. Thus, the decrease of *LUC* and *GUS* transgenic siRNAs could result from the compromised DRB4/DCL2/4 activity in *fve-8* (Fig. 5, A, B, and D). The result also explained that the reduction of transgenic siRNAs in *fve-cas9-hpCHS* mutants should attribute to the compromised DRB4/DCL2/4 activity in the absence of FVE (Fig. 5H and fig. S3C).

DISCUSSION

Here, we report a newly developed dual-reporter system for monitoring both miRNA- and siRNA-mediated RNA silencing. Using the system, we found FVE, a classical epigenetic component, as a new player in the transgene-PTGS pathway. We propose that FVE coordinates with SGS3 and DCL4/DRB4 function to promote the biogenesis of transgene-derived siRNAs (Fig. 9I). Several independent forms of evidence support this assertion. First, loss-of-function mutations of *FVE* compromised siRNA production from transgenic transcripts in several independent reporter lines (Fig. 5). Second,

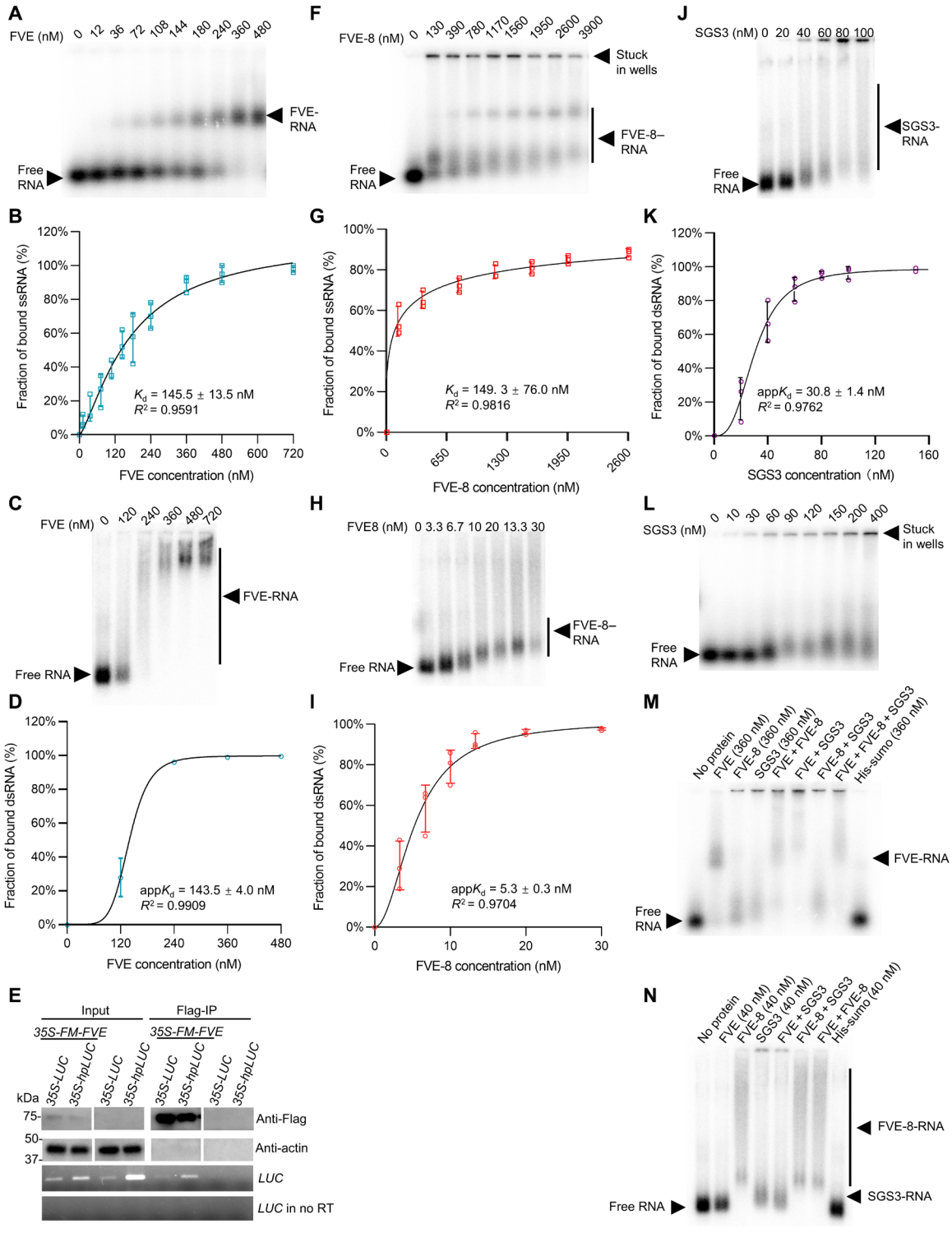

Fig. 8. EMSA showed that FVE, FVE-8, and SGS3 display different binding affinities to ssRNA and dsRNA. (**A**, **F**, and **L**) The mobility pattern of FVE (A), FVE-8 (F), and SGS3 (L) with homogenous ssRNA. Protein concentrations were shown above. Arrowheads indicate the mobility of protein-RNA complexes or free RNA. Additional repeats were shown in fig. S5. (**B** and **G**) The binding affinities (K_d and apparent K_d) of protein-ssRNA were calculated from quantification of EMSA images from (A) and (F) and additional repeats in fig. S6 with ±SD ($n = 3$). (**C**, **H**, and **J**) The mobility pattern of FVE (C), FVE-8 (H), and SGS3 (J) with dsRNA (see also fig. S6). (**D**, **I**, and **K**) The binding affinities (K_d and apparent K_d) of protein-dsRNA were calculated from quantification of EMSA images from (C, H, and J) and additional repeats in fig. S7 with ±SD ($n = 3$). (**E**) RIP assay showed that FVE binds to RNA in vivo. IP was performed with an anti-Flag antibody with the protein extracts from infiltrated *N. benthamiana* leaves. Western blot assay was performed with indicated antibodies. No RT samples served as negative controls. (**M** and **N**) EMSA showed mobility patterns of different combinations of protein-ssRNA complexes (M) and of protein-dsRNA complexes (N). His-sumo is a negative control (see also figs. S6 and S7).

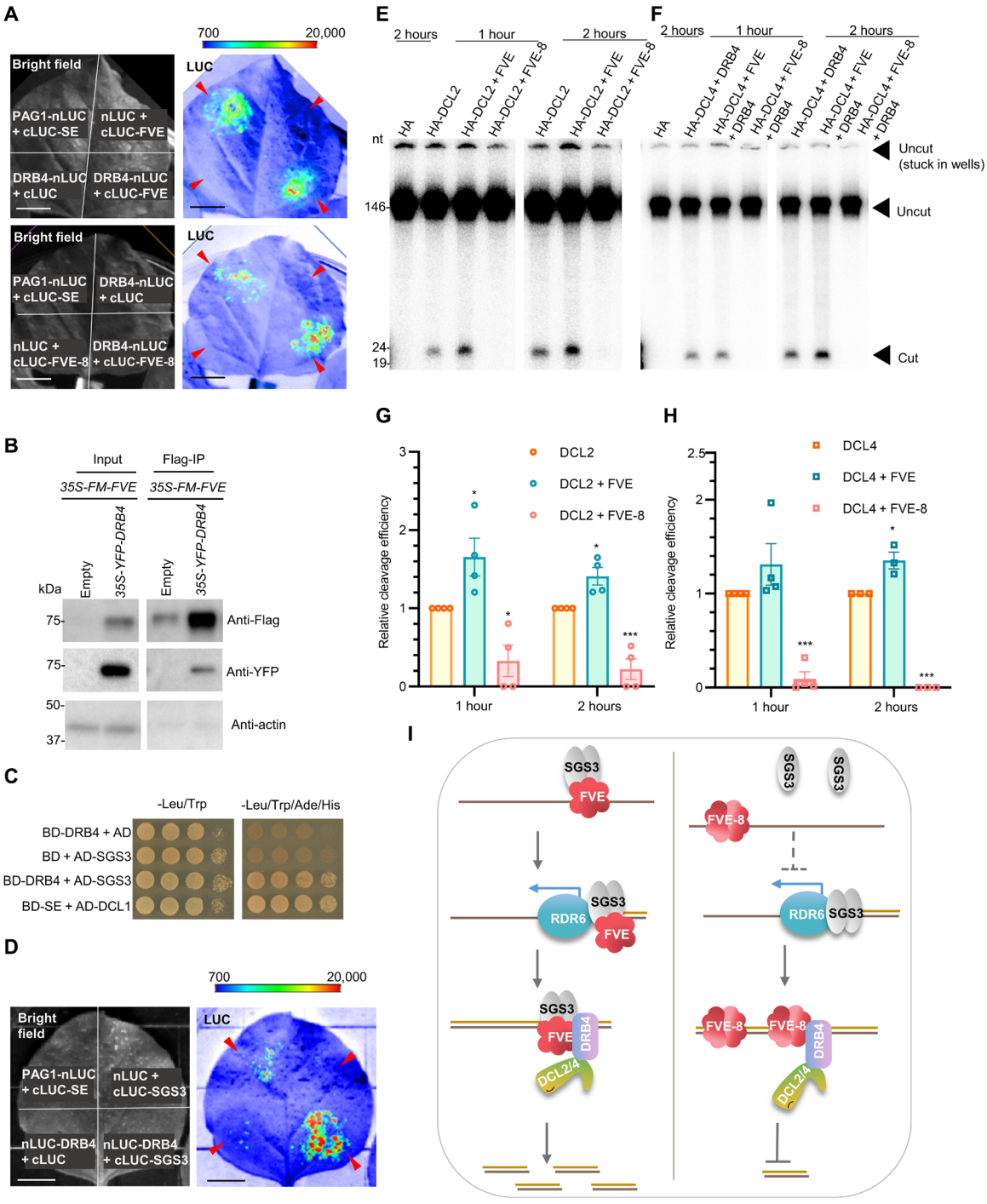

Fig. 9. In vitro reconstitution assay showed that FVE promotes whereas FVE-8 inhibits activities of DCL2/4-DRB4 complexes. (**A**) LCI assay showed that FVE (top) and FVE-8 (bottom) interact with DRB4 in *N. benthamiana*. PAG1-nLUC/cLUC-SE is a positive control (*39*). See also fig. S7. (**B**) Co-IP validated the FVE-DRB4 interaction. IP was performed with an anti-Flag antibody with the protein extracts from transfected *N. benthamiana*. Western blot assay was performed with indicated antibodies. (**C**) Y2H assay validated the DRB4-SGS3 interaction. SE/DCL1 is a positive control. (**D**) LCI assay showed that SGS3 interacts with DRB4 in *N. benthamiana*. See also fig. S7. (**E** and **F**) DCL2 (E) and DCL4 (F) dicing activity with and without FVE/FVE-8 at the indicated time points. The positions of intact substrates, processed products, and RNA markers are shown. At least three independent repeats were conducted with similar results (see also fig. S7). (**G** and **H**) Statistics of image quantitation of DCL2 (G) and DCL4 (H) activity. Individual data points are shown. **P* < 0.05; ****P* < 0.001; *t*-test. (**I**) A proposed model for FVE function in transgene silencing. FVE promotes dimerization and launching of SGS3 on ssRNA substrate, which, in turn, recruits RDR6 to produce dsRNA in vivo. Subsequently, FVE/SGS3/dsRNA is translocated to DCL4/DRB4 complexes for siRNA production. By contrast, FVE-8 does not interact with SGS3 and inefficiently promotes RDR6/SGS3 association with ssRNA substrates. Furthermore, FVE promotes DCL4/DRB4 activity, while FVE-8 sequesters dsRNA to prevent DCL4/DRB4 function in producing siRNAs.

FVE protein accumulated in the cytoplasm despite being previously thought to be exclusively in nucleus. Moreover, cytoplasmic FVE fully rescued the defect of *fve-8* in transgene silencing, indicating that the subcellular location for this function is indeed in the cytoplasm where PTGS typically occurs (Fig. 3). Third, FVE directly interacted with SGS3 and promoted its homodimerization, which represents the prerequisite for SGS3 function in PTGS (Fig. 6 and figs. S4 and S5) (*8*). Fourth, FVE bound to ssRNA substrate, whereas SGS3 barely. In this scenario, FVE might bind to ssRNA while associating with SGS3, which, in turn, recruits RDR6 for dsRNA synthesis in vivo, although this function was unnecessary in vitro. On the other hand, FVE-8 still binds to ssRNA but fails to interact with SGS3 to promote its dimerization, leading to inefficient launching of SGS3-RDR6 to ssRNA substrate in vivo (Fig. 8 and fig. S6). Fifth, given that both FVE and SGS3 interacted with DRB4, dsRNA, once generated, could be channeled from FVE/SGS3 into DRB4/DCL4 complexes for further processing to produce siRNAs. Last, FVE protein itself could directly promote the activity of DCL4/DRB4 to produce siRNAs. However, FVE-8 forms a homodimer and is granted a neo function to bind to dsRNA (Figs. 6A and 8, H and I, and fig. S7, C and D). Because FVE-8 binds to dsRNA with a significantly higher affinity than SGS3, the protein could compete with SGS3, hijack the dsRNA product, and prevent the downstream dsRNA processing by DRB4/DCL2/4 complex (Fig. 9, E to H, and fig. S8, F and G). Thus, we propose that FVE directly coordinates the two consecutive processes of transgene silencing and promotes siRNA production through its interaction with SGS3 and DRB4 as well as its RNA binding activity.

How has FVE evolved a new function in PTGS? One possibility is that FVE harbors six-tandem repeated WD40 domains. WD40 domains are widely involved in protein-protein interaction and serve as scaffolds for the assembly of large protein complexes (*41*, *42*). The presence of six WD40 domains allows FVE to partner with different targets or to shuffle between macromolecular complexes to fulfill various functions. Here, we also found two new features of FVE as a WD40 domain protein. First, WT FVE protein does not typically form oligomers, so it could create a platform or scaffold for other partners. However, the truncated variants such as FVE-8 are self-associating; correspondingly, FVE-8 homodimerization or oligomerization could block the interaction interface and, subsequently, the assembly of macromolecular complexes for proper functioning. Thus, the integrity of WD40 domains is critical for the biological roles of FVE. Second, the WD40 domain is one of the most abundant and conserved domains in eukaryotes (*41*, *42*), and emerging evidence shows that mammalian WD40 domain proteins can specifically bind to Sm site [$A(U)_{4\text{-}6}G$] and $m^7G_{ppp}G$ cap of pre–small nuclear RNAs (*43*, *44*). In addition, it has been implicated (but not confirmed) that RbAp48 may also have the potential to bind to RNA (*45*). Here, we determined that FVE binds to both ssRNA and dsRNA in a sequence-independent manner. This discovery would largely expand the spectrum of potential functions for WD40 domain–enriched proteins. Thus, the evolution of FVE to bind to RNA would allow the protein to directly modulate the functions of ribonucleoprotein complexes from SGS3/RDR6 to DRB4/DCL4.

SGS3 also exhibits several unique features that facilitate targeting by FVE. SGS3 harbors a CC domain that is essential for protein-protein interaction and homodimerization and an XS domain that is critical for RNA binding activity (*36*, *46*). SGS3 also contains a highly disordered N-terminal region with a Prion-like character (fig. S8H) (*47*, *48*). The presence of these features infers that SGS3 would have different partners and functions through various ribonucleoprotein complexes. Here, FVE promoted SGS3 dimerization, which is essential in the formation of cytoplasmic granule-like foci, called siRNA bodies (*8*). Since SGS3 and DCL4 complexes are partially colocalized (*40*), SGS3 could translocate FVE (or vice versa) to the siRNA bodies to modulate the downstream siRNA production. Notably, SGS3 has been recently reported to contribute to translocating proteasome subunits [e.g., the regulatory particle AAA-ATPase 2A (RPT2a)] into the proximity of the siRNA bodies to repress RNA quality control and to promote PTGS (*49*). Given these observations, SGS3/FVE might translocate additional presently unidentified targets to siRNA bodies for fine-tuning PTGS activities.

Many components are shared in sRNA biogenesis for endogenous RNA and foreign transcripts in PTGS. Here, SGS3 and DCL2/4 also contribute to the production of ta-siRNAs. It appears that FVE has an impact on transgene silencing but barely on endogenous RNA silencing. This scenario is also reminiscent of genes such as *JMJ14* and *RPT2a* that appear to only affect transgene siRNA production, but not the abundance of endogenous sRNAs (*49*, *50*). One plausible explanation is that the expression of transgenes, but not endogenous loci, might often lead to production of aberrant transcripts that reach the threshold of the RNA quality control machinery. Abundant transgene transcripts could be easily captured by RNA binding proteins such as FVE. Another possibility is that production of ta-siRNAs entails initial recruitment of AGO1/miR173- or AGO7/miR390-centered RISCs to *TAS* transcripts (*51*). If the identified components do not function at the interface of RDR6/SGS3-RISC, then they might not affect the production of endogenous ta-siRNAs. Of course, there might be other unknown mechanisms that would be revealed by future investigations.

In summary, we have provided conclusive evidence that FVE targets the SGS3-DCL4/DRB4 metabolism channel to promote PTGS of transgenes. An earlier report showed that the mutants of *FCA/FPA* and *FLD*, which all partner with *FVE* to regulate flowering time, can partially rescue the RNA interference (RNAi) phenotype of transgenic lines expressing *SUCROSE-PROTON SYMPORTER 2* promoter-driven hairpin transcripts of *PHYTOENE DESATURASE* (*SUC-hpPDS*). The mechanism for *fca/fpa* in rescuing *SUC-hpPDS* phenotype was interpreted through the TGS pathway (*26*). Given that FVE directly targets the SGS3/DRB4/DCL2/4 channel, it might be hypothesized that these FVE partners also directly influence SGS3/DCL4/DRB4 function. In addition, FVE and its mammalian homologs such as RbAp48 are well conserved through the eukaryotes, and whether mammalian FVE plays a similar role in RNA biology would be another exciting topic of investigation in the future.

MATERIALS AND METHODS

Experimental design

Vector construction and transgenic plants

Most of the constructs were generated by a Gateway cloning system. To obtain pENTR-GFP-PHB-LUC, a truncation form of *PHB* containing exon 4, intron 4, and exon 5 was amplified from Ler genomic DNA by *Thermococcus kodakaraenis* (KOD) DNA polymerase (Novagen). The *PHB* fragment was fused with *GFP*, *LUC*, and pENTR by DNA fragment assembly [New England Biolabs (NEB) HiFi DNA Assembly Master Mix] to generate pENTR-GFP-PHB-LUC. Then, pENTR-GFP-PHB-LUC was transferred into the Gateway compatible binary vector of pBA002a–multicloning sites (MCS)–DC by LR

Clonase (Invitrogen). *AGO10* promoter was amplified with primers P_{AGO10} For and P_{AGO10} Xho I Rev (table. S1). The PCR products were digested with Xma I and Xho I (NEB) as insert. Meanwhile, pBA002a-MCS-GFP-PHB-LUC was digested with the same enzymes as backbones. The two parts were ligated by T4 DNA ligase (NEB) and amplified by DH5α. To obtain pENTR-GFP-cPHB-LUC, a truncation form of *cPHB* containing exon 4 and exon 5 was amplified from WT cDNA by KOD DNA polymerase. After digestion with Bam HI and Kpn I, pENTR-GFP-PHB-LUC and *cPHB* fragment was ligated to get pENTR-GFP-cPHB-LUC. pENTR-GFP-cPHB-LUC was transferred into the Gateway compatible binary vector of pK-35S-FM-DC by LR Clonase. The final vectors were transformed into *Agrobacterium tumefaciens* strain ABI and then transferred to Ler *Arabidopsis* by flower dipping (*52*). Matured seeds were collected, and positive transgenic lines were selected on standard Murashige and Skoog (MS) medium containing phosphinothricin (10 mg/liter; for pBA vector; Sigma-Aldrich) or kanamycin (50 mg/liter; for pK vector; Sigma-Aldrich) together with carbenicillin (100 mg/liter; Sigma-Aldrich). Single-copy homozygous transformants were selected according to the Mendelian segregation ratio.

To obtain pK-DC-FM, pK-FM-DC was digested with Xba I and Xho I. The ends were blunted using DNA Polymerase I Large (Klenow) (NEB) and ligated to generate an intermediate vector. Then, the intermediate vector and pBA002a-DC-FM were digested with Sma I/Pac I, and the resultant fragments were ligated to generate pK-DC-FM. For the several candidate genes, full-length genomic DNAs including promoters and gene bodies were amplified by KOD DNA polymerase and were cloned into Asc I/Not I–digested pENTR vector fragment through DNA fragment assembly. For *At2g16950*, the cDNA was cloned to pENTR/D-TOPO (Invitrogen). In parallel, the promoter was ligated into the destination vector of pK-DC-FM to make pK-$P_{At2g16950}$-DC-FM. After sequencing confirmation, the pENTR-*At2g16950* vectors were transferred into a Gateway compatible binary vector of pK-$P_{At2g16950}$-DC-FM by LR Clonase (Invitrogen). The final constructs were transformed into *A. tumefaciens* strain ABI and then transferred to *fve-8* (*52*), respectively. The LUC pictures of transformants were taken on the fifth day, together with the parental line and *fve-8*. The LUC signals were reconfirmed with T_2 transgenic lines.

For pENTR-cFVE, cDNA of *FVE* with and without a stop codon was amplified by KOD DNA polymerase (Novagen) and cloned into pENTR/D-TOPO vector. The vectors were confirmed by sequencing. For pENTR-$cFVE_{NES}$, the NLS nucleotides were substituted with NES nucleotides by several steps: First, with some synonymous mutations, two restriction digestion sites (Kpn I and Bgl II; NEB) were introduced to the flanking sides of NLS by PCR with pENTR-cFVE as the template and NLS mutation Kpn I For and NLS mutation Bgl II Rev as primers (table S1). PCR products were digested with Dpn I (NEB) and transformed into *E. coli* strain DH5α. After sequencing confirmation, the new plasmid was digested with Kpn I and Bgl II. The backbone was ligated into the duplex annealed from NES For and NES Rev oligos. pENTR-cFVE and pENTR-$cFVE_{NES}$ were cloned to both pK-MCS-FM-DC and pK-35S-DC by LR Clonase. *FVE* promoter was amplified with primers P_{FVE} Bam HI For and P_{FVE} Xma I Rev (table S1). The Bam HI/Xma I–digested PCR product was ligated into the same enzyme-treated pK-MCS-FM-cFVE and pK-MCS-FM-$cFVE_{NES}$ to generate pK-P_{FVE}-FM-FVE and pK-P_{FVE}-FM-FVE_{NES}. For pK-$gFVE_{NES}$, the fragment containing the NES motif was cut from pENTR-$cFVE_{NES}$ and swapped to pK-gFVE used for complementation experiment. For pENTR-FVE-8, a coding sequence (CDS) region was amplified by KOD enzyme with cDNA from *fve-8* serving as the template. The DNA fragment containing a point mutation was replaced with the WT fragment in pENTR-FVE using Xho I and Hind III. pENTR-FVE-8 was verified by sequencing. For pENTR-FVE_{5+6}, a CDS region was amplified by KOD with cDNA from E5-4 and ligated to a pENTR vector.

For pCambia-$P_{MIR166b}$-Myc-CNA, promoter MIR166b was amplified and digested by Bam HI and Xba I. Digested fragment was ligated to the same enzyme-digested backbone of pCambia-35S-Myc-CNA (*53*). pCambia-$P_{MIR166b}$-FM-CNA, pCambia-35S-Myc-PHB(m), and pCambia-35S-Myc-PHB (*53*) were transformed into *A. tumefaciens* strains GV3101 and then transferred into E5-4 × *fve-8* F2 heterozygous lines. Positive transgenic lines were selected on MS medium with kanamycin (50 mg/liter) and hygromycin (40 mg/liter; Sigma-Aldrich), respectively. In addition, those lines were genotyped with dCAPS primers shown in table S1. The WT PCR fragment can be digested by Bam HI while that of the mutants cannot.

For CRISPR-Cas9–FVE constructs, two guide sequences targeting *FVE* were designed on the basis of (*54*). The guide sequences without protospacer adjacent motif (PAM) sequence, and its corresponding complementary strand sequences were designed to be annealed with a Bsa I–digested sticky end added at the 5′ and 3′ ends. The annealed duplexes were ligated to a Bsa I–digested AtU6-26–sgRNA (single-guide RNA) vector by T4 ligase, respectively. After sequencing confirmation, AtU6-26-sgRNA1 was digested by Spe I, and a U6-sgRNA1 fragment was recovered and ligated to fragments of AtU6-26-sgRNA2 digested by Spe I and Nhe I. The tandem sgRNA sequences were extracted from AtU6-26-sgRNA1-U6-26-sgRNA2 digestion with Spe I and Nhe I and ligated to Spe I–digested pCambia1300-pYAO-cas9-MCS. Digestion confirmed that pCambia1300-pYAO-cas9-U6-sgRNA1-U6-sgRNA2 was transformed to GV3101 and then to L1 line and *35S-hpCHS* line. T_0 plants were selected by the standard MS medium containing hygromycin B (40 mg/liter; Sigma-Aldrich) together with carbenicillin (100 mg/liter; Sigma-Aldrich). Mutation in positive plants was confirmed by sequencing.

For split-YFP constructs, full-length CDSs of FVE, FVE-8, DRB4, and SGS3 were cloned into pBA-35S-nYFP-DC and pBA-35S-cYFP-DC by the LR reaction. For split-LUC constructs, those CDSs were cloned into pCambia1300-Myc-DC-nLUC and pCambia1300-cLUC-3HA-DC by LR reaction. Digestion-confirmed plasmids were transferred to GV3101 for transit infection in tobacco leaves as described (*55*).

For Y2H vectors, full-length CDSs of FVE, SGS3, RDR6, DCL2, DCL3, DCL4, DRB4, AGO1, RDR2, and truncation FVEs were cloned into vectors pGADT7-GW and pGBKT7-GW by LR recombination. For Y3H vectors, SGS3 was amplified by PCR using a KOD hot-start DNA polymerase and digested by Bam HI and Sal I. The digested fragment was ligated to the same enzyme-digested backbone of pBridge (Clontech) vector (*5*). For pBridge-SGS3-FVE, pENTR-FVE was digested by Not I and Eco RV to obtain the FVE insert. pBridge-SGS3-MCS2 was digested by Kpn I and blunted by DNA Polymerase I Large (Klenow) and then digested by Not I to obtain the backbone. Then, the insert of FVE and the backbone were ligated by T4-ligase. For 35S-LUC and 35S-hpLUC, LUC was cloned into vectors pBA-DC and pBA-RNAi-DC by LR recombination, respectively.

For cloning of 6×His-SUMO-FVE, 6×His-SUMO–FVE-8, and 6×His-SUMO-DRB4, the CDSs of FVE, FVE-8, and DRB4 were

amplified from corresponding pENTR-FVE/FVE-8/DRB4 and ligated to pET28a-Avi-6×His-SUMO vector by Bam HI/Xho I. Sequence-confirmed plasmids were transferred to *E. coli* BL21 (DE3) cells for protein induction. For MBP-SGS3, SGS3 was cloned into vector pMAL-DC by LR recombination. For GST-6×His-SGS3 and GST-6×His-RDR6, SGS3 and RDR6 were obtained from pENTR-SGS3 and pENTR-RDR6, respectively, by digestion with Not I/Asc I. Two nucleotides were depleted between Nco I and Not I in pAcGHLT-C (BD Biosciences) to make sure the genes ligated were in frame with the GST tag. Digestion-confirmed plasmids were transfected to sf9 insect cells with baculovirus.

For cloning of 3HA-RDR6, 3HA-DCL2, and 3HA-DCL4, cDNAs of RDR6, DCL2, and DCL4 were recombined into pBA-3HA-DC to yield pBA-3HA-RDR6, pBA-3HA-DCL2, and pBA-3HA-DCL4 by LR Clonase, accordingly. Digestion-confirmed plasmids were transferred to GV3101 for transient infection in *N. benthamiana* leaves as described (*55*). Primers are listed in table S1.

Plant materials and growth conditions

A. thaliana ecotype Landsberg (Ler), Columbia (Col-0), E5-4 (Ler; PAGO10-GFP-PHB-LUC), M17-1 (Ler; 35S-GFP-cPHB-LUC), *se-2* (SAIL_44_G12), *hyl1-2* (SALK_064863), *sgs3-1, rdr6-11* (CS24285), *ago10-3* (SALK_519738), and *pnh2* (CS3853) were used for this study. Plants were grown on soil at 22°C or MS plates in 12-hour light/12-hour dark.

E5-4 was crossed with Col-0 for seven generations to get Col-0 background E5-4 (Ec5-4). Ec5-4 in *se-2*, *hyl1-2*, and *rdr6-11* background plants were obtained by crossing Ec5-4 with the mutants, respectively. M17-1 in *sgs3-1* background was obtained by crossing M17-1 with *sgs3-1*, respectively. In the F_2 generation, homozygous *rdr6-11* and *sgs3-1* mutants were identified by PCR using primers listed in table S1.

EMS mutagenesis, mutant screen, and LUC assays

EMS mutagenesis was performed as described with minor modifications (*56*). EMS (0.4%) was used to treat 20,000 seeds of E5-4 for 8 hours at room temperature. About 7000 M_1 plants survived. Approximately 56,000 5-day-old M_2 seedlings were assayed for LUC activity with an electron-multiplying charge-coupled device (CCD) camera (Princeton) and WinView 32 and LightField, of which showing enhanced LUC luminescent were picked. M_2 seedlings were outcrossed with Col-0. Genomic DNA was extracted with hexadecyltrimethylammonium bromide. Traditional mapping markers were designed on the basis of an *Arabidopsis* mapping platform. The DNA sequence library was constructed according to the manufacturer's (NEB) instructions with modifications. Next-generation sequencing was performed by Illumina, and sequence data were analyzed with SHOREmap version 2.0 (*57*) and NGM (*58*).

Aza-dc treatment

Aza-dc was dissolved in water and added to MS medium to a final concentration of 4 μM (*59*). Seeds were germinated on MS medium with or without aza for 5 days before LUC activity assay. After LUC activity was recorded, seedlings were harvested for RT-PCR.

RT-PCR and qRT-PCR

Total RNA was extracted using TRIzol (Sigma-Aldrich) from 5-day-old seedlings. Total RNA was treated with deoxyribonuclease I (DNase I; Sigma-Aldrich, AMPD1) and reverse-transcribed with SuperScript III reverse transcriptase (Invitrogen, catalog no. 18080093) primed by oligo(dT) according to the manufacturer's instructions. *Actin*, *EF1α*, or *UBQ10* genes were used as internal controls. For analysis using regular PCR, the PCR products were fractioned on agarose gels. qRT-PCR was performed using CFX384 Touch Real-Time PCR Detection System (Bio-Rad). Primers are listed in table S1.

RNA-seq and sRNA-seq

Total RNA was prepared from 5-day-old seedlings grown on MS medium using TRIzol. Construction of RNA and sRNA libraries, Illumina sequencing, and bioinformatic analysis were performed as described (*35*, *60*). The differential gene expressions analyzed in Fig. 4 (A, D, and E) and fig. S3 (A and B) are listed in table S2.

RNA blot and sRNA blot

Total RNA was extracted using TRIzol from 5-day-old seedlings (for GUS-sRNA blot in Fig. 5D, 10-day-old seedlings were used). RNA blot hybridizations of low–molecular weight RNAs (sRNA blot) and high–molecular weight RNAs (Northern blot) were performed as described previously (*32*). For miRNAs and ta-siRNA blot, the probes, which are 21-nt DNA oligos complementary to the corresponding sRNAs (the probes are listed in table S1), were labeled using [γ-^{32}P]adenosine 5′-triphosphate (ATP) (PerkinElmer) with T4 polynucleotide kinase (PNK) (NEB). For Northern blot and transgenic sRNA blot, the probes were PCR products amplified with primers listed in table. S1. Then, they were labeled using [α-^{32}P]2′-deoxycytidine 5′-triphosphate(dCTP) (PerkinElmer) with Klenow fragment (3′ to 5′ exo-; NEB). Hybridization signals were detected with Typhoon FLA 7000 (GE Healthcare).

Western blot

Western blot analyses were performed as described (*23*). Blots were detected with antibodies against Myc (Sigma-Aldrich, C 3956), YFP (Roche and Agrisera, AS15 2987), actin (Sigma-Aldrich, A0480), histone 3 (Agrisera, AS10 710), GST (Sigma-Aldrich, G-7781), AGO10 (Agrisera, AS15 3071), SGS3 (Agrisera, AS15 3099), Flag (Sigma-Aldrich, F1804), and HA (Sigma-Aldrich, H9658). Secondary antibodies were goat-developed anti-rabbit (GE Healthcare, catalog no. NA934) and anti-mouse immunoglobulin G (GE Healthcare, catalog no. NA931). Western blot membranes were developed with ECL+, and signals were detected with ChemiDoc XRS+ and captured with the Image Lab software (Bio-Rad) as per the manufacturer's instruction.

Chromatin immunoprecipitation–polymerase chain reaction

ChIP assay was performed as described (*61*). Five-day-old seedlings were harvested from MS medium. IP was developed with an anti-H3K27me3 antibody (Millipore, catalog no. 07-449) and anti-AtRPB1 (*62*). PCR primers are listed in table S1.

Nuclei RNA extraction

Well-ground powder (0.5 g) of 6-day-old seedlings of E5-4 and *fve-8* was homogenized in 5 ml of nuclei isolation buffer [0.25 M sucrose, 15 mM Pipes (pH 6.8), 5 mM $MgCl_2$, 60 mM KCl, 15 mM NaCl, 1 mM $CaCl_2$, 0.9% Triton X-100, 1 mM phenylmethylsulfonyl fluoride (PMSF), RNase In (100 U/ml), and TURBO DNase (10 U/ml)] prepared in RNase-free water for 10 min on ice. The slurry was filtered through two-layer Miracloth to a new tube. After centrifuging at 11,000*g* for 10 min at 4°C, the pallet was washed once with nucleus isolation buffer. The pellet was kept for RNA extraction using TRIzol as the nuclear RNA fraction.

Cellular localization assay and BiFC assay of YFP

Large-scale plasmid purification and protoplast transformation were performed as described (*35*). Leaves of 4-week-old plants of Col-0, E5-4, *fve-8*, and *fve-8; gFVE* were used as resources of protoplasts. Eighteen hours after transfection, fluorescence signals in the protoplast were visualized by a Leica SP8 confocal microscope (*39*). Samples

were excited by a 514-nm argon laser with an emission of 527 nm for YFP and 633 nm for chlorophyll autofluorescence, respectively. At least 10 individual protoplasts were observed with similar results for each transformation.

Nuclear-cytoplasmic fractionation assay

Five-day-old seedlings on MS medium were harvested for nuclear-cytoplasmic separation as described previously (*63*). Rubisco stained with Ponceau S and histone 3 protein level were used for fractionation quality validation and internal control.

GUS staining

F_2 seedlings of FVE (+/) and FVE (−/−) in L1 background were isolated by segregation and genotyping (primers used are listed in table S1). Ten-day-old seedlings of F_2 were harvested and developed with GUS staining as described (*5*).

Y2H and Y3H assays

Y2H and Y3H assays were performed as previously described (*5*). In the Y3H system, pBridge plasmid contains a met-suppressed promoter (*Met23* promoter) to regulate the third gene compared with Y2H system. The growing speed of transfected colonies serves as a proxy of SGS3-SGS3 homodimer amount. The constructs were cotransformed and selected on the medium lacking leucine (Leu), tryptophan (Trp), histidine (His), and methionine (Met) but supplemented with 5 mM 3-amino-1,2,4-triazole for Y3H assays. Different amounts of Met (0, 1, and 2 mM) were added to the medium to regulate the transcription activity of *Met23* promoter. Note that yeast colonies tend to grow faster in the medium with the nutrient Met than the one without Met (Fig. 6E and fig. S5C). At least 10 independent colonies were tested for each combination, and they all showed similar results.

LCI assay

LCI assays were performed as previously described (*61*). For each LCI assay, at least three individual leaves were observed with similar results.

Coimmunoprecipitation

For Co-IP in Fig. 6B, 10-day-old Ler and *fve-8; P_{FVE}-FM-cFVE* seedlings were harvested and ground well in liquid nitrogen, respectively. Powder (0.5 g) was homogenized in 2.5 ml of IP buffer [50 mM tris-HCl (pH 7.6), 150 mM NaCl, 5 mM $MgCl_2$, 0.1% Triton X-100, 1% glycerol, 2 mM PMSF, 5 mM dithiothreitol (DTT), one pellet per 15 ml of IP buffer EDTA-free proteinase inhibitor (Roche), and 50 μM MG132] and mixed well for 10 min on ice. The total protein extracts were centrifuged at 15,000 rpm for 15 min at 4°C twice. After total proteins were extracted, anti-Flag M2 magnetic beads (Sigma-Aldrich, M8823) were added to extracts and incubated at 4°C for 2 hours. For RNase A treatment, RNase A (0.05 mg/ml) was added to the IP buffer before incubation. After incubation, beads were washed four times with wash buffer [20 mM tris-HCl (pH 7.6), 100 mM NaCl, 0.05% Tween 20, 2 mM DTT, and one pellet per 15 ml of buffer EDTA-free proteinase inhibitor (Roche)] at 4°C for 5 min. The beads were boiled in 2× SDS protein loading buffer for 10 min before Western blot analysis. An anti-Flag antibody was used to detect IP products, and an anti-SGS3 antibody was used to determine the coprecipitation levels of SGS3. For Co-IP in Fig. 8E, after 48 hours of infection, infiltrated *N. benthamiana* leaves and mock leaves were harvested and cross-linked in buffer [0.4 M sucrose, 10 mM tris-HCl (pH 8.0), 1 mM PMSF, 1 mM EDTA, and 1% formaldehyde] for 10 min by vacuum infiltration. The reaction was stopped with a final concentration of 100 mM glycine. The samples were rinsed four times with ice-cold water and ground well in liquid nitrogen, respectively. Powder (0.3 g) was homogenized in 1.1 ml of IP buffer [40 mM tris-HCl (pH 7.6), 150 mM NaCl, 5 mM $MgCl_2$, 75 μM $ZnCl_2$, 0.1% Triton X-100, 0.1% glycerol, 2 mM PMSF, 5 mM DTT, one pellet per 15 ml of IP buffer EDTA-free proteinase inhibitor (Roche), and 15 μM MG132] for 10 min on ice. The total protein extracts were centrifuged at 15,000 rpm for 15 min at 4°C twice. After the total proteins were extracted, anti-Flag M2 magnetic beads (Sigma-Aldrich, M8823) were added to the extracts for the enrichment of Flag-tagged protein at 4°C for 2 hours. After incubation, the beads were washed four times with the IP buffer at 4°C for 5 min. The beads were boiled in 2× SDS protein loading buffer for 10 min before Western blot. An anti-Flag antibody was used to detect IP products, and an anti-YFP antibody was used to detect coimmunoprecipitates.

Expression and purification of recombinant proteins

Protein expression and purification were performed as described in (*5*) with modifications. 6×His-SUMO-FVE, 6×His-SUMO-FVE-8, MBP-SGS3, and 6×His-SUMO-DRB4 were expressed in *E. coli* BL21 (DE3) cells. GST-6×His-SGS3, GST-6×His-RDR6, and GST-6×His-DCL4 were expressed in a baculovirus/insect cell expression system. For recombinant proteins expressed in *E. coli*, transformed BL21 cells were grown in LB at 37°C until the optical density at 600 nm is equal to 0.6. Then, the expression was induced with 0.5 mM isopropyl-β-D-thiogalactopyranoside at 37°C for 3 hours.

For purification of FVE, the induced bacterial cells were collected and resuspended in lysis buffer [40 mM tris-HCl buffer (pH 8.0), 300 mM KCl, 2% glycerol, 1 mM β-mercaptoethanol, 1 mM PMSF, and 0.1% Triton X-100]. Cells were disrupted using LM20 Digital Microfluidizer Processor at 25,000 psi for three cycles. The disrupted cells were centrifuged at 18,000 rpm for 15 min at 4°C. The supernatant was filtered with a 0.45-μm filter and made up to 20 mM imidazole and 1% Triton X-100. The cleared lysate was loaded onto a HisTrap HP column (GE Healthcare, catalog no. 17-5248-02). The column was washed with 25 ml of wash buffer [40 mM tris-HCl (pH 8.0), 300 mM KCl, 2% glycerol, 1 mM β-mercaptoethanol, 1 mM PMSF, and 80 mM imidazole] and eluted with gradient elution buffer from 80 to 300 mM imidazole [40 mM tris-HCl (pH 8.0), 300 mM KCl, 2% glycerol, 1 mM β-mercaptoethanol, and 1 mM PMSF]. The peak fractions of the recombinant protein were pooled and dialyzed in dialysis tubing with 10-kDa–molecular weight cutoff (MWCO) stirring in dialysis buffer [20 mM tris-HCl (pH 7.5), 60 mM KCl, 2% glycerol, 2 mM β-mercaptoethanol, 2 mM DTT, and 140 nM SUMO protease] at 4°C overnight. The uncut recombinant protein was removed by Ni beads. The fractions were concentrated by a 30-kDa-MWCO Centricon (Millipore, catalog no. Z71785) and loaded onto a HiLoad 16/600 Superdex 200 pg column (GE Healthcare). The gel filtration buffer contained 20 mM tris-HCl (pH 7.5), 60 mM KCl, 2 mM β-mercaptoethanol, and 2 mM DTT. The peak fractions containing FVE were collected and dialyzed in dialysis tubing with 10-kDa-MWCO stirring in dialysis buffer [20 mM tris-HCl (pH 7.5), 60 mM KCl, 2 mM β-mercaptoethanol, 2 mM DTT, and 50% glycerol] at 4°C overnight. The final dialysate was aliquoted and frozen by liquid nitrogen and stored at −80°C. The purifications of FVE-8 and DRB4 are similar to that of FVE. MBP-SGS3 is purified as described in (*61*).

For purification of recombinant protein in insect cells, pAcGHLT-GST-6×His vectors were transfected with BaculoGold baculovirus DNA system (BD Biosciences, catalog no. 554740) into sf9 insect cells (BD Biosciences, catalog no. 554738; authenticated by the vendor BD Biosciences) to generate recombinant baculovirus. After two rounds

of viruses were amplified, P3 virus was collected for large-scale protein expression (*5*).

For GST-6×His-SGS3, the P3 virus was added to 2.5×10^6 sf9 insect cells/ml for propagation, and the insect cells were collected 65 hours later. Insect cells were resuspended in lysis buffer [40 mM tris-HCl (pH 8.0), 500 mM NaCl, 5% glycerol, 1 mM β-mercaptoethanol, 1 mM PMSF, 0.1% Triton X-100, and 1× proteinase inhibitor (Sigma-Aldrich)] and disrupted with LM20 Digital Microfluidizer Processor at 5000 psi for 2 cycles. Disrupted cells were centrifuged at 20,000 rpm for 30 min at 4°C. The supernatant was filtered with a 0.45-μm filter and made up to 20 mM imidazole and 1% Triton X-100. The cleared lysate was loaded onto a HisTrap FF column (GE Healthcare). The column was washed with 25 ml of wash buffer [40 mM tris-HCl (pH 8.0), 500 mM NaCl, 5% glycerol, 1 mM β-mercaptoethanol, 1 mM PMSF, and 40 mM imidazole] and eluted with gradient elution buffer from 40 to 300 mM imidazole [40 mM tris-HCl (pH 8.0), 500 mM NaCl, 5% glycerol, 1 mM β-mercaptoethanol, and 1 mM PMSF]. The peak fractions of recombinant protein were pooled and dialyzed in dialysis tubing with 10-kDa-MWCO stirring in dialysis buffer [40 mM tris-HCl (pH 8.0), 500 mM NaCl, 5% glycerol, 1 mM β-mercaptoethanol, 1 mM DTT, and 1 mM PMSF] at 4°C for 4 hours. The fractions were collected and loaded onto a GSTrap HP column (GE Healthcare, catalog no. 17-528201). The column was washed with 25 ml of wash buffer [40 mM tris-HCl (pH 7.5), 500 mM NaCl, 5% glycerol, 1 mM β-mercaptoethanol, and1 mM DTT] and eluted with gradient elution buffer from 0 to 15 mM reduced glutathione [40 mM tris-HCl (pH 8.0), 500 mM NaCl, 5% glycerol, 1 mM β-mercaptoethanol, and 1 mM DTT]. The peak fractions were concentrated by 50-kDa-MWCO Centricon (Millipore, catalog no. UFC905024) and then dialyzed in dialysis tubing with 10-kDa-MWCO stirring in dialysis buffer [40 mM tris-HCl (pH 8.0), 150 mM NaCl, 1 mM β-mercaptoethanol, 1 mM DTT, 2 mM PMSF, and 50% glycerol] at 4°C for 6 hours. The final dialysate was aliquoted and frozen by liquid nitrogen and stored at −80°C. Similarly, GST-6×His-RDR6 was purified and dialyzed in dialysis buffer [20 mM Hepes-KOH (pH 7.6), 20 mM NaCl, 0.2 mM EDTA, 2 mM β-mercaptoethanol, and 50% glycerol] at 4°C for 6 hours. The final dialysate was aliquoted and frozen by liquid nitrogen and stored at −80°C.

In vitro pull-down assay

In vitro pull-down assay was performed as described (*61*). MBP-SGS3 was used as a bait protein, and GST-tagged proteins were used as prey proteins.

In vitro transcription and labeling of RNA

For in vitro transcription, 5′ end and body labeling of RNA substrates were performed as described (*4*). The substrate of ssRNA (AT1TE45390) for RNA-dependent RNA polymerase (RdRP) assay is a PCR fragment amplified from a **pEGM-t-easy** vector containing the T7 promoter, followed by the transposon sequence as described (*35*). The substrate of ssRNA for EMSA is G3A44 synthesized by T7 in vitro transcription (*55*). For the dsRNA used in EMSA and DCL assay, two PCR fragments were amplified from LUC coding region (363 to 509 nt) with primers shown in table. S1. A sense RNA strand and an antisense strand were transcribed by T7 in vitro transcriptase with [α-^{32}P]uridine 5′-triphosphate (UTP) (3000 Ci/mmol) as internal labeling, respectively.

RdRP reconstitution assay

For in vitro RdRP assay, 20 μl of reaction mixtures containing 50 mM Hepes-KOH (pH 7.6), 20 mM NH_4OAc, 2% (w/v) PEG4000 (polyethylene glycol, molecular weight 4000), 16 mM $MgCl_2$, 0.1 mM EDTA, 0.1 mM ATP, 0.1 mM CTP, 0.1 mM guanosine triphosphate (GTP), 0 to 50 μM UTP, and 0 to 0.5 μM [a-^{32}P]UTP (3000 Ci/mmol), SUPERaseIn (1 U/μl), and 2 pmol of each recombinant protein except RDR6 were mixed as indicated and preincubated on ice for 20 min. ssRNA template (10 pmol) was added to each reaction and incubated for 30 min. RDR6 (1 pmol) was added to each sample and to initiate the reaction at room temperature for 20 min, respectively. The samples were digested with proteinase K for 30 min at 37°C. Samples were purified with phenol-chloroform and fractionated on 6% urea-polyacrylamide gel. The RDR6 product was visualized by radiography. The experiments were repeated three times for statistical analysis. The semi–in vitro RdRP reconstitution assay was performed as described (*34*, *35*) with modifications. Reaction mixtures (20 μl) containing 50 mM Hepes-KOH (pH 7.6), 20 mM NH_4OAc, 2% (w/v) PEG4000, 16 mM $MgCl_2$, 0.1 mM EDTA, 1 mM ATP, 1 mM CTP, 1 mM GTP, 0.1 mM UTP, 0.5 μM [a-^{32}P]UTP (3000 Ci/mmol), 10 pmol of ssRNA template, SUPERaseIn (1 U/μl), and recombinant proteins were mixed and preincubated on ice for 30 min. Then, 3 μl of HA beads containing HA-RDR6 were added to each sample and to initiate reaction at room temperature for 0.5, 1, and 1.5 hours, respectively. Samples were boiled with urea loading buffer and fractionated on 6% urea-polyacrylamide gel. The final result was visualized by radiography.

Electrophoretic mobility shift assays

EMSA was performed as described with modifications (*5*). Recombinant proteins were mixed in the EMSA buffer [10 mM tris-HCl (pH 7.5), 4% glycerol, 1 mM $MgCl_2$, 0.2 mM EDTA, and 0.5 mM DTT]. The mixture was incubated on ice for 30 min before labeled RNA was added. For dsRNA EMSA, RNA was denatured at 95°C for 3 min in buffer [100 mM KCl and 30 mM tris-HCl (pH 7.5)] and slowly cooled down to room temperature. The mixtures were incubated at room temperature for 30 min. Bound complexes were resolved on a native agarose gel. The gel was incubated in fixing buffer (40% ethanol, 10% acetic acid, and 5% glycerol) for 15 min and dried at 80°C for 2 hours and then visualized by radiography. The K_d and appK_d were calculated using Prism GraphPad 8 software fit with a Hill slope model.

Ribonucleoprotein complex IP (RIP) RT-PCR

For RIP, after 48 hours of infection, infiltrated *N. benthamiana* leaves were harvested and cross-linked as described in the "Coimmunoprecipitation" section. Powder (0.5 g) was homogenized in 2.5 ml of RIP buffer [40 mM tris-HCl (pH 7.5), 100 mM KCl, 5 mM $MgCl_2$, 0.2% Triton X-100, 0.1% glycerol, 1 mM PMSF, 5 mM DTT, one pellet per 15 ml of IP buffer EDTA-free proteinase inhibitor (Roche), 15 μM MG132, RNase In (100 U/ml), and TURBO DNase (10 U/ml)] prepared in RNase-free water for 10 min on ice. The total protein extracts were centrifuged at 15,000 rpm for 15 min at 4°C twice. After proteins were extracted, balanced anti-Flag M2 magnetic beads were added to the extracts for Flag tag enrichment at 4°C for 2 hours. After incubation, the beads were washed twice with RIP buffer and twice with high-salt buffer [40 mM tris-HCl (pH 7.5), 500 mM KCl, 5 mM $MgCl_2$, 5 mM DTT, 0.2% Triton X-100, 2% glycerol, 1 mM PMSF, 25 μM MG132, and one pellet per 10 ml of cOmplete EDTA-free protease inhibitor] at 4°C for 5 min, followed by one-time wash with proteinase K buffer [50 mM tris-HCl (pH 7.5), 200 mM NaCl, 10 mM EDTA, and 1% SDS]. The beads were treated with proteinase K (2 mg/ml) in 150 μl of proteinase K buffer at 65°C overnight. One share of beads was boiled in 2× SDS protein loading buffer for 10 min before Western blot. Anti-Flag antibody was used to detect

IP. The other share of beads was used for RNA extraction. After TURBO DNase digestion, reverse transcription was performed as described in the "RT-PCR and qRT-PCR" section except primed with random primers. Primers used for PCR are listed in table S1.

In vitro DCL2/4 assay

HA-DCL2/4 IP assay was performed with a modified protocol from DCL1 IP (*4*). After 48 hours of infection, infiltrated *N. benthamiana* leaves and mock leaves were harvested and ground well in liquid nitrogen, respectively. Powder (0.5 g) was homogenized in 2.5 ml of IP buffer [40 mM tris-HCl (pH 7.5), 300 mM KCl, 5 mM $MgCl_2$, 0.2 mM EDTA (pH 8.0), 5 mM DTT, 0.2% Triton X-100, one pellet per 15 ml of IP buffer EDTA-free proteinase inhibitor (Roche), 1 mM PMSF, and 2% glycerol] for 10 min on ice. After total proteins were extracted, anti-HA agarose beads (Sigma-Aldrich, A2095) were used for HA tag enrichment at 4°C for 2 hours. After incubation, the beads were washed four times with wash buffer [20 mM tris-HCl (pH 7.5), 1 mM DTT, 4 mM $MgCl_2$, and 100 mM KCl] at 4°C for 5 min. The final beads were stored with 7 volumes of DCL storage buffer [20 mM tris-HCl (pH 7.5), 1 mM DTT, 4 mM $MgCl_2$, and 20% glycerol] and stored at −20°C before use. 1 pmol of FVE, 1 pmol of FVE-8, and 1 pmol of SGS3 (for DCL4 assay, 1 pmol of DRB4 was also added) were added to a 20-μl reaction system, respectively, as needed, containing 1000 counts per minute of ^{32}P-labeled dsRNA substrates, 20 mM tris-HCl (pH 7.5), 4 mM $MgCl_2$, 1 mM DTT, 5 mM ATP, 1 mM GTP, and SUPERaseIn RNase Inhibitor (1 U/μl; Invitrogen). The mixture above was homogenized on ice for 30 min. The assay was initiated by adding 3.5 μl of HA-IP products as indicated and tumbling at 25°C at 1000 rpm in a thermomixer. HA-IP product from mock *N. benthamiana* serves as a negative control. The reactions were stopped by 1% SDS and proteinase K (2 mg/ml) digestion at 37°C for 30 min. After phenol-chloroform purification, DCL-processed products were fractionated using 12% denaturing polyacrylamide gel and detected with a phosphor imaging plate (GE Healthcare).

Statistical analysis

For RNA-seq and sRNA-seq, an edgeR (version 3.3) package was used to normalize gene expression levels with trimmed mean of M-values according to the false discovery rate (*60*). The cutoff for significance was 0.05.

Quantification of Northern blot, Western blot, EMSAs, RdRP assays, and DCL2/4 assays was performed by measuring the intensity of the bands by ImageJ 1.52 software. For EMSAs and RdRP assays, the curves were fitted, and the values were calculated using GraphPad prism 8.

For qRT-PCR and confocal foci statistics, the data were presented as means of at least three replicates ±SD. For Figs. 2 (B and E) and 3D, the relative expression of tested genes was initially normalized to that of *EF-1α* (Figs. 2B and 3D) and *UBQ10* (Fig. 2E) and then to WT (E5-4) where the ratio was arbitrarily assigned a value of 1 with ±SD (n = 3) biologically independent replicates. For DCL2/4 assays, the histogram was presented as the mean of three or four replicates ± SEM.

Unpaired two-tailed Student's t test was performed to calculate the P value. The cutoff for significance was 0.05. *P < 0.05, **P < 0.01, and ***P < 0.001.

SUPPLEMENTARY MATERIALS

Supplementary material for this article is available at http://advances.sciencemag.org/cgi/content/full/7/32/eabf3898/DC1

View/request a protocol for this paper from *Bio-protocol*.

REFERENCES AND NOTES

1. D. P. Bartel, Metazoan microRNAs. *Cell* **173**, 20–51 (2018).
2. S. Li, C. Castillo-González, B. Yu, X. Zhang, The functions of plant small RNAs in development and in stress responses. *Plant J.* **90**, 654–670 (2017).
3. Z. Ma, X. Zhang, Actions of plant Argonautes: Predictable or unpredictable? *Curr. Opin. Plant Biol.* **45**, 59–67 (2018).
4. H. Zhu, Y. Zhou, C. Castillo-Gonzalez, A. Lu, C. Ge, Y. T. Zhao, L. Duan, Z. Li, M. J. Axtell, X. J. Wang, X. Zhang, Bidirectional processing of pri-miRNAs with branched terminal loops by *Arabidopsis* Dicer-like1. *Nat. Struct. Mol. Biol.* **20**, 1106–1115 (2013).
5. Z. Wang, Z. Ma, C. Castillo-González, D. Sun, Y. Li, B. Yu, B. Zhao, P. Li, X. Zhang, SWI2/SNF2 ATPase CHR2 remodels pri-miRNAs via Serrate to impede miRNA production. *Nature* **557**, 516–521 (2018).
6. T. Dalmay, A. Hamilton, S. Rudd, S. Angell, D. C. Baulcombe, An RNA-dependent RNA polymerase gene in *Arabidopsis* is required for posttranscriptional gene silencing mediated by a transgene but not by a virus. *Cell* **101**, 543–553 (2000).
7. P. Mourrain, C. Béclin, T. Elmayan, F. Feuerbach, C. Godon, J. B. Morel, D. Jouette, A.-M. Lacombe, S. Nikic, N. Picault, K. Rémoué, M. Sanial, T.-A. Vo, H. Vaucheret, *Arabidopsis SGS2* and *SGS3* genes are required for posttranscriptional gene silencing and natural virus resistance. *Cell* **101**, 533–542 (2000).
8. T. Elmayan, X. Adenot, L. Gissot, D. Lauressergues, I. Gy, H. Vaucheret, A neomorphic *sgs3* allele stabilizing miRNA cleavage products reveals that SGS3 acts as a homodimer. *FEBS J.* **276**, 835–844 (2009).
9. M. Yoshikawa, T. Iki, Y. Tsutsui, K. Miyashita, R. S. Poethig, Y. Habu, M. Ishikawa, 3′ fragment of miR173-programmed RISC-cleaved RNA is protected from degradation in a complex with RISC and SGS3. *Proc. Natl. Acad. Sci. U.S.A.* **110**, 4117–4122 (2013).
10. M. Yoshikawa, A. Peragine, M. Y. Park, R. S. Poethig, A pathway for the biogenesis of *trans*-acting siRNAs in *Arabidopsis*. *Genes Dev.* **19**, 2164–2175 (2005).
11. H. Nagano, A. Fukudome, A. Hiraguri, H. Moriyama, T. Fukuhara, Distinct substrate specificities of *Arabidopsis* DCL3 and DCL4. *Nucleic Acids Res.* **42**, 1845–1856 (2014).
12. J. S. Parent, N. Bouteiller, T. Elmayan, H. Vaucheret, Respective contributions of *Arabidopsis* DCL 2 and DCL 4 to RNA silencing. *Plant J.* **81**, 223–232 (2015).
13. M. Tijsterman, R. F. Ketting, R. H. A. Plasterk, The genetics of RNA silencing. *Annu. Rev. Genet.* **36**, 489–519 (2002).
14. J. S. Parent, V. Jauvion, N. Bouche, C. Beclin, M. Hachet, M. Zytnicki, H. Vaucheret, Post-transcriptional gene silencing triggered by sense transgenes involves uncapped antisense RNA and differs from silencing intentionally triggered by antisense transgenes. *Nucleic Acids Res.* **43**, 8464–8475 (2015).
15. R. Harmoko, W. I. D. Fanata, J. Y. Yoo, K. S. Ko, Y. G. Rim, M. N. Uddin, T. A. Siswoyo, S. S. Lee, D. Y. Kim, S. Y. Lee, K. O. Lee, RNA-dependent RNA polymerase 6 is required for efficient hpRNA-induced gene silencing in plants. *Mol. Cells* **35**, 202–209 (2013).
16. E. Nicolas, V. Morales, L. Magnaghi-Jaulin, A. Harel-Bellan, H. Richard-Foy, D. Trouche, RbAp48 belongs to the histone deacetylase complex that associates with the retinoblastoma protein. *J. Biol. Chem.* **275**, 9797–9804 (2000).
17. S. Kosmidis, A. Polyzos, L. Harvey, M. Youssef, C. A. Denny, A. Dranovsky, E. R. Kandel, RbAp48 protein is a critical component of GPR158/OCN signaling and ameliorates age-related memory loss. *Cell Rep.* **25**, 959–973.e6 (2018).
18. Y. Sunagawa, M. Funamoto, K. Shimizu, S. Shimizu, Y. Katanasaka, Y. Miyazaki, H. Wada, K. Hasegawa, T. Morimoto, P4998 novel GATA4 binding proteins, RbAp48/46, regulate cardiomyocyte hypertrophy with depending on the phosphorylate State of GATA4. *Eur. Heart J.* **40**, ehz746.0176 (2019).
19. I. Ausin, C. Alonso-Blanco, J. A. Jarillo, L. Ruiz-Garcia, J. M. Martinez-Zapater, Regulation of flowering time by FVE, a retinoblastoma-associated protein. *Nat. Genet.* **36**, 162–166 (2004).
20. H. J. Kim, Y. Hyun, J. Y. Park, M. J. Park, M. K. Park, M. D. Kim, H. J. Kim, M. H. Lee, J. Moon, I. Lee, J. Kim, A genetic link between cold responses and flowering time through FVE in *Arabidopsis thaliana*. *Nat. Genet.* **36**, 167–171 (2004).
21. S. F. Abou-Elwafa, B. Buttner, T. Chia, G. Schulze-Buxloh, U. Hohmann, E. Mutasa-Gottgens, C. Jung, A. E. Muller, Conservation and divergence of autonomous pathway genes in the flowering regulatory network of *Beta vulgaris*. *J. Exp. Bot.* **62**, 3359–3374 (2011).
22. I. Baurle, C. Dean, Differential interactions of the autonomous pathway RRM proteins and chromatin regulators in the silencing of *Arabidopsis* targets. *PLOS ONE* **3**, e2733 (2008).
23. H. Zhu, F. Hu, R. Wang, X. Zhou, S. H. Sze, L. W. Liou, A. Barefoot, M. Dickman, X. Zhang, *Arabidopsis* Argonaute10 specifically sequesters miR166/165 to regulate shoot apical meristem development. *Cell* **145**, 242–256 (2011).
24. Y. Zhou, M. Honda, H. Zhu, Z. Zhang, X. Guo, T. Li, Z. Li, X. Peng, K. Nakajima, L. Duan, X. Zhang, Spatiotemporal sequestration of miR165/166 by *Arabidopsis* Argonaute10 promotes shoot apical meristem maintenance. *Cell Rep.* **10**, 1819–1827 (2015).
25. X. Gu, D. Jiang, W. Yang, Y. Jacob, S. D. Michaels, Y. He, *Arabidopsis* homologs of retinoblastoma-associated protein 46/48 associate with a histone deacetylase to act redundantly in chromatin silencing. *PLOS Genet.* **7**, e1002366 (2011).

26. I. Baurle, L. Smith, D. C. Baulcombe, C. Dean, Widespread role for the flowering-time regulators FCA and FPA in RNA-mediated chromatin silencing. *Science* **318**, 109–112 (2007).
27. M. Pazhouhandeh, J. Molinier, A. Berr, P. Genschik, MSI4/FVE interacts with CUL4-DDB1 and a PRC2-like complex to control epigenetic regulation of flowering time in *Arabidopsis*. *Proc. Natl. Acad. Sci. U.S.A.* **108**, 3430–3435 (2011).
28. H. Stroud, M. V. C. Greenberg, S. Feng, Y. V. Bernatavichute, S. E. Jacobsen, Comprehensive analysis of silencing mutants reveals complex regulation of the *Arabidopsis* methylome. *Cell* **152**, 352–364 (2013).
29. M. Brameier, A. Krings, R. M. MacCallum, NucPred—Predicting nuclear localization of proteins. *Bioinformatics* **23**, 1159–1160 (2007).
30. R. Ye, W. Wang, T. Iki, C. Liu, Y. Wu, M. Ishikawa, X. Zhou, Y. Qi, Cytoplasmic assembly and selective nuclear import of *Arabidopsis* Argonaute4/siRNA complexes. *Mol. Cell* **46**, 859–870 (2012).
31. S. V. Wesley, C. A. Helliwell, N. A. Smith, M. B. Wang, D. T. Rouse, Q. Liu, P. S. Gooding, S. P. Singh, D. Abbott, P. A. Stoutjesdijk, S. P. Robinson, A. P. Gleave, A. G. Green, P. M. Waterhouse, Construct design for efficient, effective and high-throughput gene silencing in plants. *Plant J.* **27**, 581–590 (2001).
32. X. Zhang, Y.-R. Yuan, Y. Pei, S.-S. Lin, T. Tuschl, D. J. Patel, N.-H. Chua, *Cucumber mosaic virus*-encoded 2b suppressor inhibits *Arabidopsis* Argonaute1 cleavage activity to counter plant defense. *Genes Dev.* **20**, 3255–3268 (2006).
33. N. Kumakura, A. Takeda, Y. Fujioka, H. Motose, R. Takano, Y. Watanabe, SGS3 and RDR6 interact and colocalize in cytoplasmic SGS3/RDR6-bodies. *FEBS Lett.* **583**, 1261–1266 (2009).
34. J. Curaba, X. Chen, Biochemical activities of *Arabidopsis* RNA-dependent RNA polymerase 6. *J. Biol. Chem.* **283**, 3059–3066 (2008).
35. Z. Ma, C. Castillo-González, Z. Wang, D. Sun, X. Hu, X. Shen, M. E. Potok, X. Zhang, *Arabidopsis* Serrate coordinates histone methyltransferases ATXR5/6 and RNA processing factor RDR6 to regulate transposon expression. *Dev. Cell* **45**, 769–784.e6 (2018).
36. R. Fukunaga, J. A. Doudna, dsRNA with 5′ overhangs contributes to endogenous and antiviral RNA silencing pathways in plants. *EMBO J.* **28**, 545–555 (2009).
37. A. Fukudome, T. Fukuhara, Plant Dicer-like proteins: Double-stranded RNA-cleaving enzymes for small RNA biogenesis. *J. Plant Res.* **130**, 33–44 (2017).
38. M. Clavel, T. Pelissier, J. Descombin, V. Jean, C. Picart, C. Charbonel, J. Saez-Vasquez, C. Bousquet-Antonelli, J. M. Deragon, Parallel action of AtDRB2 and RdDM in the control of transposable element expression. *BMC Plant Biol.* **15**, 70 (2015).
39. Y. Li, D. Sun, Z. Ma, K. Yamaguchi, L. Wang, S. Zhong, X. Yan, B. Shang, Y. Nagashima, H. Koiwa, J. Han, Q. Xie, M. Zhou, Z. Wang, X. Zhang, Degradation of SERRATE via ubiquitin-independent 20S proteasome to survey RNA metabolism. *Nat. Plants* **6**, 970–9821-13 (2020).
40. O. Pontes, A. Vitins, T. S. Ream, E. Hong, C. S. Pikaard, P. Costa-Nunes, Intersection of small RNA pathways in *Arabidopsis thaliana* sub-nuclear domains. *PLOS ONE* **8**, e65652 (2013).
41. C. U. Stirnimann, E. Petsalaki, R. B. Russell, C. W. Müller, WD40 proteins propel cellular networks. *Trends Biochem. Sci.* **35**, 565–574 (2010).
42. C. Xu, J. Min, Structure and function of WD40 domain proteins. *Protein Cell* **2**, 202–214 (2011).
43. W. Jin, Y. Wang, C.-P. Liu, N. Yang, M. Jin, Y. Cong, M. Wang, R.-M. Xu, Structural basis for snRNA recognition by the double-WD40 repeat domain of Gemin5. *Genes Dev.* **30**, 2391–2403 (2016).
44. C. Xu, H. Ishikawa, K. Izumikawa, L. Li, H. He, Y. Nobe, Y. Yamauchi, H. M. Shahjee, X.-H. Wu, Y.-t. Yu, T. Isobe, N. Takahashi, J. Min, Structural insights into Gemin5-guided selection of pre-snRNAs for snRNP assembly. *Genes Dev.* **30**, 2376–2390 (2016).
45. M. Bellucci, F. Agostini, M. Masin, G. G. Tartaglia, Predicting protein associations with long noncoding RNAs. *Nat. Methods* **8**, 444–445 (2011).
46. D. Zhang, V. L. Trudeau, The XS domain of a plant specific SGS3 protein adopts a unique RNA recognition motif (RRM) fold. *Cell Cycle* **7**, 2268–2270 (2008).
47. M. E. Oates, P. Romero, T. Ishida, M. Ghalwash, M. J. Mizianty, B. Xue, Z. Dosztányi, V. N. Uversky, Z. Obradovic, L. Kurgan, A. Keith Dunker, J. Gough, D^2P^2: Database of disordered protein predictions. *Nucleic Acids Res.* **41**, D508–D516 (2012).
48. A. K. Lancaster, A. Nutter-Upham, S. Lindquist, O. D. King, PLAAC: A web and command-line application to identify proteins with prion-like amino acid composition. *Bioinformatics* **30**, 2501–2502 (2014).
49. M. H. Kim, J. Jeon, S. Lee, J. H. Lee, L. Gao, B. H. Lee, J. M. Park, Y. J. Kim, J. M. Kwak, Proteasome subunit RPT2a promotes PTGS through repressing RNA quality control in *Arabidopsis*. *Nat. Plants* **5**, 1273–1282 (2019).
50. I. R. Searle, O. Pontes, C. W. Melnyk, L. M. Smith, D. C. Baulcombe, JMJ14, a JmjC domain protein, is required for RNA silencing and cell-to-cell movement of an RNA silencing signal in *Arabidopsis*. *Genes Dev.* **24**, 986–991 (2010).
51. E. Allen, Z. Xie, A. M. Gustafson, J. C. Carrington, microRNA-directed phasing during trans-acting siRNA biogenesis in plants. *Cell* **121**, 207–221 (2005).
52. X. Zhang, R. Henriques, S.-S. Lin, Q.-W. Niu, N.-H. Chua, *Agrobacterium*-mediated transformation of *Arabidopsis thaliana* using the floral dip method. *Nat. Protoc.* **1**, 641–646 (2006).
53. S. Li, L. Liu, X. Zhuang, Y. Yu, X. Liu, X. Cui, L. Ji, Z. Pan, X. Cao, B. Mo, F. Zhang, N. Raikhel, L. Jiang, X. Chen, MicroRNAs inhibit the translation of target mRNAs on the endoplasmic reticulum in *Arabidopsis*. *Cell* **153**, 562–574 (2013).
54. H. Liu, Y. Ding, Y. Zhou, W. Jin, K. Xie, L.-L. Chen, CRISPR-P 2.0: An improved CRISPR-Cas9 tool for genome editing in plants. *Mol. Plant* **10**, 530–532 (2017).
55. Z. Zhang, F. Hu, M. W. Sung, C. Shu, C. Castillo-González, H. Koiwa, G. Tang, M. Dickman, P. Li, X. Zhang, RISC-interacting clearing 3′-5′exoribonucleases (RICEs) degrade uridylated cleavage fragments to maintain functional RISC in *Arabidopsis thaliana*. *eLife* **6**, e24466 (2017).
56. W. Wang, R. Ye, Y. Xin, X. Fang, C. Li, H. Shi, X. Zhou, Y. Qi, An importin β protein negatively regulates microRNA activity in *Arabidopsis*. *Plant Cell* **23**, 3565–3576 (2011).
57. K. Schneeberger, S. Ossowski, C. Lanz, T. Juul, A. H. Petersen, K. L. Nielsen, J. E. Jorgensen, D. Weigel, S. U. Andersen, SHOREmap: Simultaneous mapping and mutation identification by deep sequencing. *Nat. Methods* **6**, 550–551 (2009).
58. H. Li, J. Ruan, R. Durbin, Mapping short DNA sequencing reads and calling variants using mapping quality scores. *Genome Res.* **18**, 1851–1858 (2008).
59. O. Mathieu, J. Reinders, M. Čaikovski, C. Smathajitt, J. Paszkowski, Transgenerational stability of the *Arabidopsis* epigenome is coordinated by CG methylation. *Cell* **130**, 851–862 (2007).
60. D. Sun, Z. Ma, J. Zhu, X. Zhang, Identification and quantification of small RNAs, in *Arabidopsis Protocols* (Springer, 2021), pp. 225–254.
61. C. Castillo-Gonzalez, X. Liu, C. Huang, C. Zhao, Z. Ma, T. Hu, F. Sun, Y. Zhou, X. Zhou, X.-J. Wang, X. Zhang, Geminivirus-encoded TrAP suppressor inhibits the histone methyltransferase SUVH4/KYP to counter host defense. *eLife* **4**, e06671 (2015).
62. A. Fukudome, D. Sun, X. Zhang, H. Koiwa, Salt stress and CTD PHOSPHATASE-LIKE4 mediate the switch between production of small nuclear RNAs and mRNAs. *Plant Cell* **29**, 3214–3233 (2017).
63. Z. Zhang, X. Guo, C. Ge, Z. Ma, M. Jiang, T. Li, H. Koiwa, S. W. Yang, X. Zhang, KETCH1 imports HYL1 to nucleus for miRNA biogenesis in *Arabidopsis*. *Proc. Natl. Acad. Sci. U.S.A.* **114**, 4011–4016 (2017).

Acknowledgments: We thank X. Chen for pCambia-35S-PHB/PHBm-Myc plasmids, R. Klein and S. Rodrigues for careful editing, and Zhang Lab members for discussion and proofreading of this manuscript. **Funding:** The work was supported by grants from NIH R01GM127742 and NSF (MCB-1716243) to X.Z. D.S. and X.Y. were partially supported by the China Scholar Council fellowship. **Author contributions:** X.Z. conceived the project. D.S., Z.M., and X.Z. designed the study. D.S. and Y.L. performed the experiments. Z.M. conducted bioinformatics analysis. X.Y. conducted protein purification. N.L. verified the EMS-reporter system of M17-1. H.K. guided initial CCD-based screening, provided RPB1 antibody, and edited the manuscript. B.S. performed confocal experiments. X.H. conducted part of sRNA blot assays. K.C. did part of genotyping. D.S. and Y.L. analyzed the data. D.S. and X.Z. wrote the paper. **Competing interests:** The authors declare that they have no competing interests. **Data and materials availability:** The data generated during this study have been deposited in GEO under the series reference of GSE171316. All other data needed to evaluate the conclusions in the paper are present in the paper and/or the Supplementary Materials. Additional data related to this paper may be requested from the authors.

Submitted 22 October 2020
Accepted 15 June 2021
Published 4 August 2021
10.1126/sciadv.abf3898

Citation: D. Sun, Y. Li, Z. Ma, X. Yan, N. Li, B. Shang, X. Hu, K. Cui, H. Koiwa, X. Zhang, The epigenetic factor FVE orchestrates cytoplasmic SGS3-DRB4-DCL4 activities to promote transgene silencing in *Arabidopsis*. *Sci. Adv.* **7**, eabf3898 (2021).

The epigenetic factor FVE orchestrates cytoplasmic SGS3-DRB4-DCL4 activities to promote transgene silencing in *Arabidopsis*

Di Sun, Yanjun Li, Zeyang Ma, Xingxing Yan, Niankui Li, Baoshuan Shang, Xiaomei Hu, Kai Cui, Hisashi Koiwa and Xiuren Zhang

Sci Adv **7** (32), eabf3898.
DOI: 10.1126/sciadv.abf3898